Electronic Supplementary Material (ESI) for Physical Chemistry Chemical Physics.

A Theoretical Spectroscopy Study of the Photoluminescent Properties of Narrow Band Eu^{2+}-doped Phosphors Containing Multiple Candidate Doping Centers. Prediction of an Unprecedented Narrow Band Red phosphor

Rami Shafei, Philipp Jean Strobel, Peter J. Schmidt, Dimitrios Maganas,*

Wolfgang Schnick* and Frank Neese*

Supplementary Material

S I. Embedded Cluster Approach

For the studied systems (RNLSO, RNLSO2 and CBLA2), the crystal structures' coordinates are taken form the crystallographic data, refined based on the experimental crystallographic X-ray diffraction. For CBLA, the crystal structure is built by transformation of CBLA2 to tetragonal space group, the cell parameters are optimized using CRYSTAL package[1, 2], and this primarily optimized coordinates will be used to build the CBLA clusters.

All the clusters were constructed on the basis of the embedded cluster approach, where the quantum clusters (QCs) are embedded in a point charge (PC) field of about 15000 charges which account for the long-range Coulomb effects of the solid. One HF layer and three effective core potentials ECP layers are introduced between the QC and PCs to avoid 1) highly negatively charged QCs and 2) spurious electron leakage and over-delocalization of the QC, respectively. The HF layer atoms are treated with smaller basis set (LANL2DZ) with HayWadt pseudopotentials[3-6]. Generally, the QC neutralization region (HF region) is treated at the same computational level used for the QC except when QC is treated at the coupled cluster (CC) level, this region is treated at the Hartree-Fock level of theory. In the ECPs region the corresponding crystallographic positions are substituted by repulsive capped effective core potentials (c-ECPs). The employed types of ECPs are ECP2SDF for (Li)[7], ECP2MWB for (O, N)[8], ECP10SDF for (Na, Mg)[7], ECP10MBW for (Al, Si, Ca)[8, 9], ECP28MDF for (Rb)[10], and ECP46MBW for (Ba)[9], as included in the SDD framework.

The chosen charges to equip the ECP and PC regions were chosen on the basis of electrostatic potential charges (CHELPG)[11, 12] iterative optimization step in the framework of the Ionic-Crystal-QMMM embedded cluster protocol in ORCA. The chosen convergence criteria ensure an overall neutral cluster according to the neutrality condition ($q(QC + HF) = -q(BR + PC)$)[13] as well as a uniform charge distribution in all (QC, HF, BR, and PC) regions.
For cluster size convergence, discussed in section S II, a series of cluster models were built in a sequence of size growing ranging from monomers, dimers, trimers, tetramers, and pentamers, as shown in Figure S1. For the study set all this information is collectively presented in Figure S1 and Table S1.

Table S1. Description of the employed Eu^{2+}-doped clusters within the embedded cluster approach in terms of 1) the QCs composition, 2) HF layers 3) the number of atoms in the ECP region, 4) the number of points in the PC region and 5) the converged CHELPG charges of ECPs and PCs. An Eu-doped cluster is constructed by replacing one doping site, (Na^+ /Rb^+/Ca^{2+} /Ba^{2+}) cation.

Phosphor	Doping site	Cluster Size	QC	HF	n(cECP)	n(PC)	CHELPG Charges
$RbNa_3[Li_3SiO_4]_4:Eu^{2+}$ RNLSO	$Na(1)^+$	1	$[EuLi_8O_{20}]^{30-}$	$[Rb_2Na_6Li_8Si_4]^{32}$	232	16886	Rb:1.62, Na:0.92, Si: 2.62, Li: 1.17, O: -2.09
		2	$[EuRbLi_{12}O_{28}]^{41-}$	$[RbNaLi_8Si_8]^{42}$	254	16864	
		3	$[EuRb_2Li_{16}O_{36}]^{52-}$	$[Na_{14}Li_8Si_8]^{54}$	314	16768	
		4	$[EuRb_2NaLi_{20}O_{44}]^{63-}$	$[RbNa_3Li_{12}Si_{12}]^{64}$	342	16740	
		5	$[EuRb_2Na_2Li_{24}O_{52}]^{74-}$	$[Rb_2Na_{10}Li_{16}Si_{12}]^{76}$	396	16650	
	$Na(2)^+$	1	$[EuLi_4Si_4O_{20}]^{18-}$	$[Rb_3Na_5Li_{12}]^{20}$	200	16918	Rb:1.55, Na:1.04, Si: 2.78, Li: 1.20, O: -2.06
		2	$[EuNaLi_6Si_6O_{28}]^{23-}$	$[Rb_2Na_6Li_{16}]^{24}$	230	16932	
		3	$[EuNa_2Li_8Si_8O_{36}]^{28-}$	$[Rb_4Na_6Li_{20}]^{30}$	274	16808	
		4	$[EuNa_3Li_{10}Si_{10}O_{44}]^{33-}$	$[Rb_2Na_8Li_{24}]^{34}$	310	16816	
		5	$[EuNa_4Li_{12}Si_{12}O_{52}]^{38-}$	$[Rb_5Na_7Li_{28}]^{40}$	348	16698	
	Rb^+	1	$[EuLi_8O_{20}]^{30-}$	$[Na_{10}Li_4Si_4]^{30}$	230	16878	Rb:1.53, Na:0.99, Si: 2.66, Li: 1.13, O: -2.00
		2	$[EuNaLi_{12}O_{28}]^{41-}$	$[RbNaLi_8Si_8]^{42}$	254	16864	
		3	$[EuNa_2Li_{16}O_{36}]^{52-}$	$[Rb_2Na_8Li_{12}Si_8]^{54}$	314	16756	
		4	$[EuRbNa_2Li_{20}O_{44}]^{63-}$	$[RbNa_3Li_{12}Si_{12}]^{64}$	342	16740	
		5	$[EuRb_2Na_2Li_{24}O_{52}]^{74-}$	$[Na_{16}Li_{12}Si_{12}]^{76}$	396	16638	
$RbNa[Li_3SiO_4]_2:Eu^{2+}$ RNLSO2	Na^+	1	$[EuLi_4Si_4O_{20}]^{18-}$	$[Rb_4Na_2Li_{12}]^{18}$	192	16428	Rb:1.47, Na:0.90, Si: 2.74, Li: 1.13, O: -2.21
		2	$[EuNaLi_6Si_6O_{28}]^{23-}$	$[Rb_6Na_2Li_{16}]^{24}$	230	16454	
		3	$[EuNa_2Li_8Si_8O_{36}]^{28-}$	$[Rb_8Na_2Li_{20}]^{30}$	274	16308	
		4	$[EuNa_3Li_{10}Si_{10}O_{44}]^{33-}$	$[Rb_8Na_2Li_{24}]^{34}$	310	16338	
		5	$[EuNa_4Li_{12}Si_{12}O_{52}]^{-38}$	$[Rb_8Na_2Li_{28}]^{38}$	346	16202	
	Rb^+	1	$[EuLi_8O_{20}]^{30-}$	$[Rb_2Na_8Li_6Si_4]^{32}$	232	16318	Rb:1.56, Na:1.00, Si: 2.81, Li: 1.18, O: -2.17
		2	$[EuRbLi_{12}O_{28}]^{41-}$	$[Rb_2Na_2Li_6Si_8]^{42}$	260	16402	
		3	$[EuRb_2Li_{16}O_{36}]^{52-}$	$[Rb_2Na_{12}Li_8Si_8]^{54}$	314	16200	
		4	$[EuRb_3Li_{20}O_{44}]^{63-}$	$[Rb_2Na_2Li_{12}Si_{12}]^{64}$	342	16284	
		5	$[EuRb_4Li_{24}O_{52}]^{74-}$	$[Rb_2Na_4Li_{14}Si_{14}]^{76}$	384	16100	
$CaBa[LiAl_3N_4]_2$ CBLA2	Ba^{2+}	1	$[EuLi_4Al_4N_{20}]^{42-}$	$[Ca_8Ba_2Al_8]^{44}$	224	15228	Ba:1.87, Ca:1.63, Al: 1.93, Li: 0.88, N: -2.36
		2	$[EuBaLi_6Al_6N_{28}]^{56-}$	$[Ca_2Ba_2Al_{16}]^{56}$	256	15086	
		3	$[EuBa_2Li_8Al_8N_{36}]^{70-}$	$[Ca_4Ba_2Al_{20}]^{72}$	298	15120	
		4	$[EuBa_3Li_{10}Al_{10}N_{44}]^{84-}$	$[Ca_4Ba_2Al_{24}]^{84}$	344	14962	
		5	$[EuBa_4Li_{12}Al_{12}N_{52}]^{98-}$	$[Ca_6Ba_2Al_{28}]^{100}$	386	14996	
	Ca^{2+}	1	$[EuAl_8N_{20}]^{34-}$	$[Ca_2Ba_4Li_6Al_6]^{36}$	192	15264	Ba:1.77, Ca:1.63, Al: 1.93, Li: 0.93, N: -2.27
		2	$[EuCaAl_{12}N_{28}]^{44-}$	$[Ca_2Ba_4Li_8Al_8]^{44}$	234	15096	
		3	$[EuCa_2Al_{16}N_{36}]^{54-}$	$[Ca_2Ba_8Li_6Al_{10}]^{56}$	272	15150	
		4	$[EuCa_3Al_{20}N_{44}]^{64-}$	$[Ca_2Ba_{12}Li_{12}Al_8]^{64}$	314	14978	
		5	$[EuCa_4Al_{24}N_{52}]^{74-}$	$[Ca_2Ba_8Li_{14}Al_{14}]^{76}$	346	15038	
$Ca_3Ba[LiAl_3N_4]_4$ CBLA	Ba^{2+}	3	$[EuCa_2Li_8Al_{20}N_{48}]^{70-}$	$[Ba_2Li_6Al_{20}]^{70}$	319	15556	Ba: 1.85, Ca: 1.44, Al: 1.99, Li: 1.13, N: -2.15
	$Ca(1)^{2+}$	3	$[EuBa_2Li_4Al_{24}N_{48}]^{62-}$	$[Ca_2Li_8Al_{17}]^{63}$	306	15552	
	$Ca(2)^{2+}$	3	$[EuCa_2Li_8Al_{20}N_{48}]^{70-}$	$[Ca_6Ba_4Li_2Al_{16}]^{70}$	352	15484	

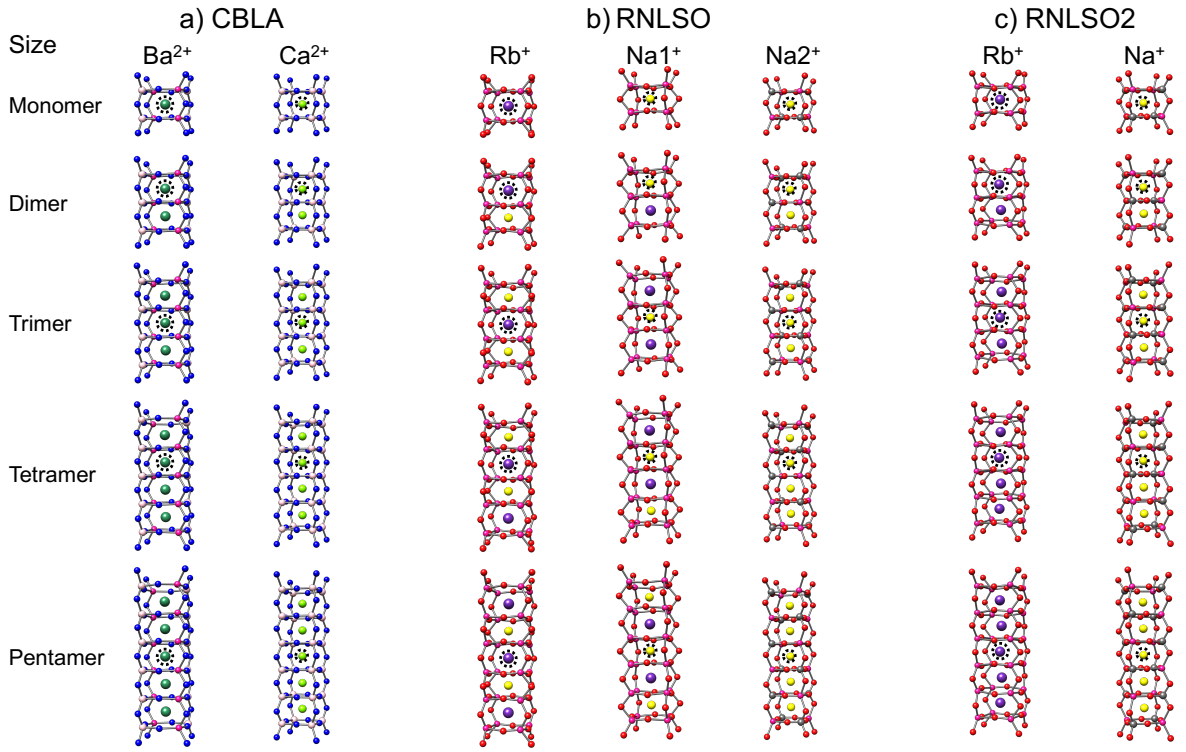

Figure S1. All cluster models (QCs) for a) CBLA2 (Ca^{2+} and Ba^{2+} channels), b) RNLSO (Rb^{+}, $Na(1)^{+}$, $Na(2)^{+}$ channels), c) RNLSO2 (Rb^{+} and Na^{+} channels). Different sized models named with respect to number (n) of the central metal ion (Ca^{2+}, Ba^{2+}, Rb^{+}, Na^{+}) in the cluster as (Monomer, Dimer, Trimer, Tetramer, Pentamer for n=1, 2, 3, 4, 5, respectively). The Eu^{2+} doping site is indicated with dotted black circle around the ion that will be replaced by Eu^{2+}. Atom colors: Rb (purple), Na (yellow), Ca (light green), Ba (deep green), Si (dark gray), Al (yellowish pink), Li (pink), N (blue), O (red).

S II. Cluster Size Convergence – Choice of the Computational Protocol

Initially, it is essential to identify the minimum cluster size that encapsulates all relevant electronic structure information and the most efficient computational protocol (DFT functional) in both the host and doped materials. For, each probable doping center, the optical band gap of the host structures were calculated by the similarity transformed equation of motion domain-based local pair natural orbital coupled cluster singles and doubles (STEOM-

DLPNO-CCSD)[14, 15] as well as TD-DFT[16] methods. In the latter, a collection of DFT functionals were chosen, belonging to the GGA: PBE,[17] hybrid: PBE0,[18-20] range separated hybrid: CAM-B3LYP,[21] double hybrid: B2PLYP,[22] and range separated double hybrid: ωB2PLYP[23] families. Similarly, TD-DFT and canonical open-shell EOM-CCSD[24] were employed to compute the band gap energies of the Eu^{2+}-doped structures.

As a first step the cluster size convergence is evaluated on the basis of the optical band gap (BG) energies of the host structures. As has been described previously, [25] the optical band gap is defined as the lowest optically allowed electronic excitation energy.

As seen in Figure S2, the lowest excitation energies in the host, for all employed functionals, were converged at the trimer cluster size. In the case of the CBLA clusters the lowest excitation energy (optical BG) is observed for the clusters containing Ba^{2+} centers while in the case of RNLSO and RNLSO2 clusters the lowest excitation energy (optical BG) is observed for the clusters containing Na^{+} centers.

As shown Table S2 and Figures S2-3, in comparison to the available experimental data[26, 27] the computed values show significant underestimations and non-systematic deviations ranging between ~15500-37500 cm^{-1} (1.9-4.6 eV). In contrast, as has been observed previously[25, 28] the situation changes rapidly when STEOM-DLPNO-CCSD is employed to compute the BG energies (Figure S3). In the case of RNLSO and RNLSO2 the MAE errors drop below 0.03 eV in comparison to the available experimental data. Hence in a next step STEOM-DLPNO-CCSD is employed to evaluate the performance of the various DFT functionals. Table S2 shows that in comparison to the STEOM-DLPNO-CCSD computed values MAE decreases in the sequence PBE, PBE0, CAM-B3LYP, B2PLYP and ωB2PLYP (MAE=4.6, 3.1, 2.4, 3.0, and 1.9 eV, respectively). This general failure of TD-DFT to computed the BG energies of these systems is not surprising[29] as in fact they reflect non-rigid $O^{2-} - 2p \rightarrow Na^{+} - 3s$ (for RNLSO and RNLSO2) and $N^{3-} - 2p \rightarrow Ba^{2+} - 5d$ (for CBLA2) ligand to metal charge transfer (LMCT) transitions. This is shown in Figure S4 for RNLSO as a collective representative example, where experimental optical band gap can reproduced only on STEOM-DLPNO-CCSD level of theory on the trimer cluster.

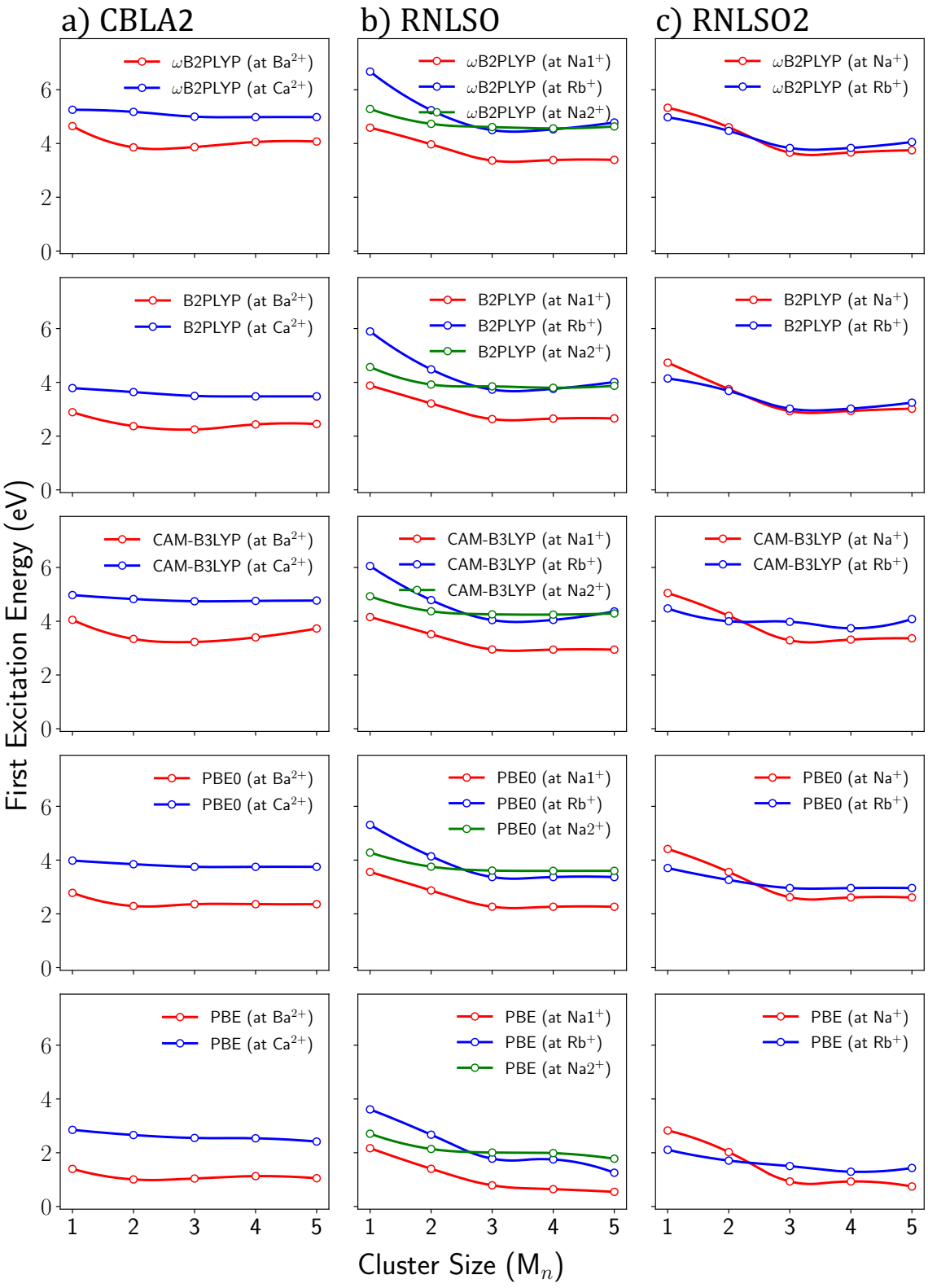

Figure S2. TD-DFT computed first excitation energies (eV) of the hosts for the variety undoped QC sizes (n = 1: monomers, 2: dimers, 3: trimers, 4: tetramers, 5: pentamers) across the employed study set of phosphors, a) CBLA2 (at Ba^{2+} site in red and at Ca^{2+} site blue), b) RNLSO (at $Na(1)^{+}$ site in red, at Rb^{+} site in blue, and at $Na(2)^{+}$ site in green), c) RNLSO2 (at

Na^+ site in red and at Rb^+ site in blue). The following DFT functionals were employed, ωB2PLYP (1st row), B2PLYP (2nd row) CAM-B3LYP (3rd row), PBE0 (4th row) and PBE (5th row).

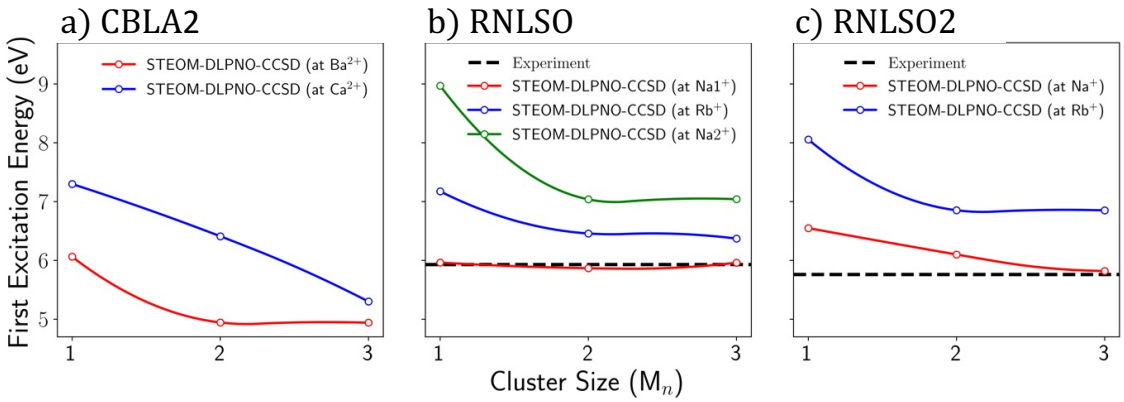

Figure S3. STEOM-DLPNO-CCSD computed first excitation energies (eV) of the hosts, for the variety undoped QC sizes (n = 1: monomers, 2: dimers, 3: trimers), across the employed study set of phosphors, a) CBLA2 (at Ba^{2+} site in red and at Ca^{2+} site blue), b) RNLSO (at Na^+ site in red, at Rb^+ site in blue, and at $Na(2)^+$ site in green), c) RNLSO2 (at Na^+ site in red and at Rb^+ site in blue). In the case of RNLSO, RNLSO2 black dotted lines represent the available experimental optical band gap energies[26, 27].

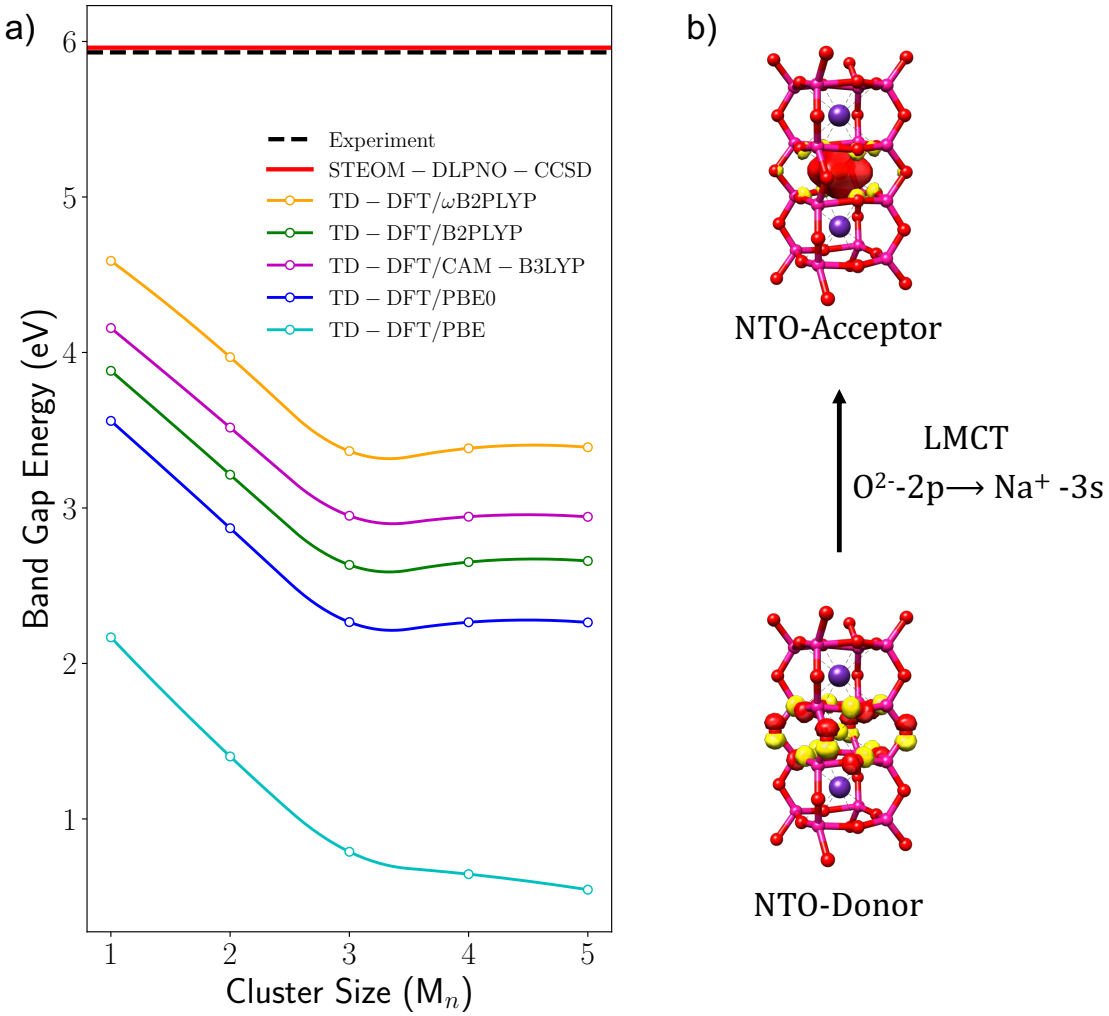

Figure S4. a) Experimental (black) and calculated optical band gap, Eg (eV) with TD-DFT/ PBE (cyan), PBE0 (blue), CAM-B3LYP (pink), B2PLYP (green) and ωB2PLYP (orange) at different size of undoped QC clusters (1: monomer, 2: dimer, 3: trimer, 4: tetramer, 5: pentamer) and with STEOM-DLPNO-CCSD (red) at the trimer cluster for RNLSO. b) The nature of the first excitation in RNLSO at central $Na(1)^{+}$ based on NTO analysis.

Table S2. Calculated band gap (BG) of trimer clusters of CBLA2, RNLSO, and RNLSO2 phosphors' hosts using TD-DFT/ PBE, PBE0, CAM-B3LYP, B2PLYP and ωB2PLYP as well as using STEOM-DLPNO-CCSD. The calculated optical BG energy is chosen as the lowest first excitation energies across different metal centers per host (Figure S3-4) and compared with available measured experimental BG. All values are in cm^{-1}, and also in eV in parentheses.

Phosphor's Host	Central cation	Calc. optical band gap in cm^{-1} (eV)						Exp. band gap cm^{-1} (eV)
		TD-DFT					STEOM-DLPNO-CCSD	
		PBE	PBE0	CAM-B3LYP	B2PLYP	ωB2PLYP		
$CaBa[LiAl_3N_4]_2$ CBLA2	Ba^{2+}	8388 (1.04)	19035 (2.36)	26052 (3.23)	18147 (2.25)	31214 (3.87)	39844 (4.94)	--
$RbNa_3[Li_3SiO_4]_4$ RNLSO	$Na(1)^+$	6372 (0.79)	18309 (2.27)	23793 (2.95)	21212 (2.63)	12582 (1.56)	48071 (5.96)	47829 (5.93)
$RbNa[Li_3SiO_4]_2$ RNLSO2	Na^+	7501 (0.93)	21132 (2.62)	26536 (3.29)	23632 (2.93)	29520 (3.66)	46941 (5.82)	46458 (5.76)
*MAE		37289 (4.62)	25218 (3.13)	19249 (2.39)	23712 (2.94)	15405 (1.91)	241 (0.03)	

*MAE are calculated with respect to the experiment, except for CBLA2, due to lack of experimental BG, STEOM-DLPNO-CCSD is taken as a reference.

In a next step, the first excitation energies of the Eu^{2+}-doped phosphors were computed at the various doping centers at the TD-DFT and the canonical open shell CASSCF(7,19)/NEVPT2/SOC levels of theory employing the monomer clusters. The results are presented in Table S3.

Table S3. The first excitation energies (in cm^{-1}) calculated using TD-DFT employing various functionals (PBE, PBE0, CAM-B3LYP, B2PLYP, and ωB2PLYP) as well as CASSCF(7,19)/NEVPT2 for the smallest Eu^{2+}-doped embedded clusters (monomers, n=1). All the probable doping site was tested Ba^{2+}/Ca^{2+} and Na^{+}/Rb^{+} for CBLA2 and both RNLSO and RNLSO2, respectively. The energy shift (in cm^{-1}) of the TD/DFT computed first excited state energy form the respective CASSCF-NEVPT2 energy is shown in parentheses. In the last two rows, the mean absolute errors MAE and the mean absolute deviations MAE(%) of the computed first excited state are presented taking the computed CASSCF/NEVPT2 energies as reference.

Phosphor	Doping site	1st Excitation Energy (cm^{-1})					
		PBE	PBE0	CAM-B3LYP	B2PLYP	ωB2PLYP	CASSCF/ NEVPT2
$CaBa[LiAl_3N_4]_2:Eu^{2+}$ CBLA2	Ba^{2+}	12406 (8773)	21601 (-422)	21764 (-585)	14537 (6642)	16118 (5061)	21179
	Ca^{2+}	3807 (8561)	12170 (198)	11998 (370)	5142 (7226)	7343 (5025)	12368
$RbNa_3[Li_3SiO_4]_4:Eu^{2+}$ RNLSO	$Na(1)^{+}$	16402 (5880)	22104 (178)	22072 (210)	16664 (5618)	17687 (4595)	22282
	$Na(2)^{+}$	13052 (6886)	20876 (-938)	19192 (746)	12669 (7269)	14853 (5085)	19938
	Rb^{+}	24621 (4248)	29242 (-373)	28481 (388)	23181 (5688)	23657 (5212)	28869
$RbNa[Li_3SiO_4]_2:Eu^{2+}$ RNLSO2	Na^{+}	12680 (7023)	20586 (-883)	18895 (808)	12431 (7272)	14656 (5047)	19703
	Rb^{+}	12803 (10039)	22237 (605)	21294 (1548)	15181 (7661)	16521 (6321)	22842

MAE	7344.3	513.7	665.0	6768.0	5192.3	--
MAE (%)	34.9	2.4	3.2	32.2	24.7	--

By comparing the various TD-DFT computed energies against the EOM-CCSD values, which are taken as a reference, the situation with respect to the undoped phosphors is changing drastically. GGA and double hybrid functionals outperform showing MAE values which range between ~ 5000-7000 cm^{-1} (0.62-0.87 eV) from the reference EOM-CCSD values. In contrast, the hybrid functionals (PBE0, CAM-B3LYP) show noticeable smaller deviations when compared against the EOM-CCSD computed values, MAE ~ 500-700 cm^{-1} (0.06-0.09 eV). This is due to the different nature of the probed transition. In the case of the undoped phosphors the transitions that dominates the BG energies are of LMCT character while in the case of the Eu^{2+}-doped ones they have a rigid $4f \rightarrow 5d$ character. This implies that hybrid functionals (PBE0 or CAM-B3LYP) are indeed good candidates for targeting the absorption and photoluminescence properties of the study set of Eu^{2+}-doped phosphors.

In a last step based on its performance the PBE0 hybrid functional is employed to compute the absorption spectra of the study set of the Eu^{2+}-doped phosphors in the sequence monomer to pentamer clusters. The results are presented in Figure S5 showing once again that in all studied cases the TD-DFT/PBE0 computed spectra converge for the trimer cluster size. Provided that the spectra are shifted by $\sim 500 - 700\ cm^{-1}$, the computed spectra are also in satisfactory visual agreement to experiment in terms of the number and the relative intensities of the computed bands.

Based of the above results and in an effort to stay consistent with our previous study on narrow band Eu^{2+}-doped phosphors,[28] in the following sections the trimer structures are chosen for the production calculations and analysis of the absorption and emission processes employing the TD-DFT/PBE0 computational protocol in conjunction with the excited state dynamics (ESD).

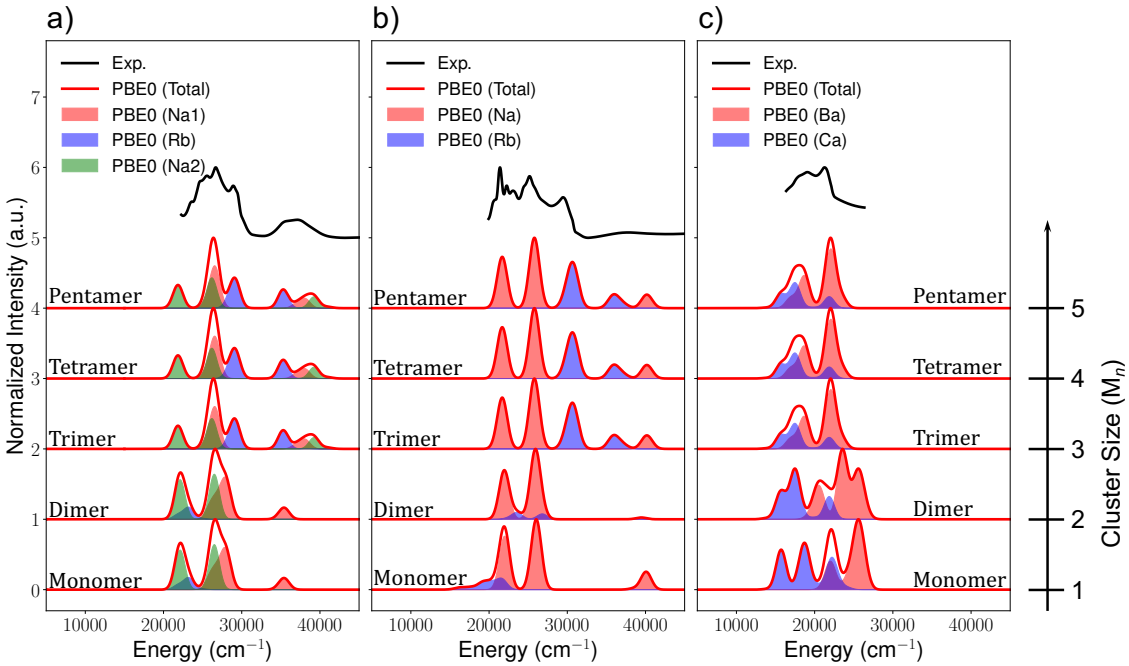

Figure S5. Experimental (in black) and TD-DFT PBE0 calculated (in red) absorption spectra at different size doped QC (monomers, dimers, trimers, tetramers, and pentamers) for a) RNLSO (Na(1) site in pale red, Rb site in pale blue, and Na(2) site in pale green fill), b) RNLSO2 (Na site in pale red and Rb site in pale blue fill) and c) CBLA2 (Ba site in pale red and Ca site pale blue fill). A shift between 500-700 cm-1 is applied to spectra for agreement to the experimental spectra.

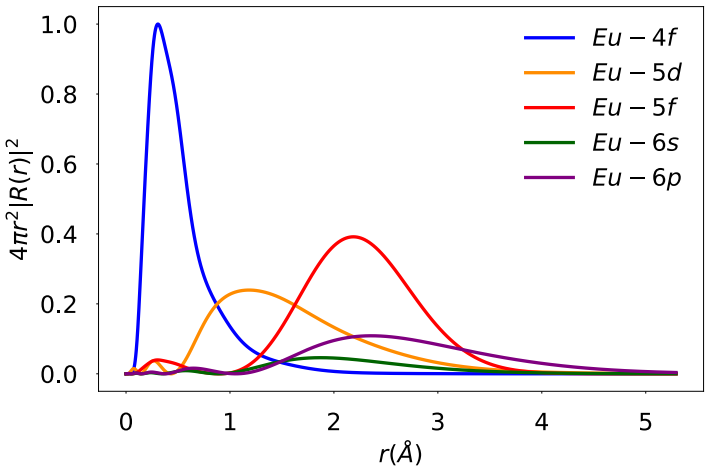

Figure S6a. Radial wavefunction $(4\pi r^2|R(r)|^2)$ as a function of r for Eu^{2+} (4f, 5d, 5f, 6s, 6p) shells in embedded $[EuN_8]^{22-}$.

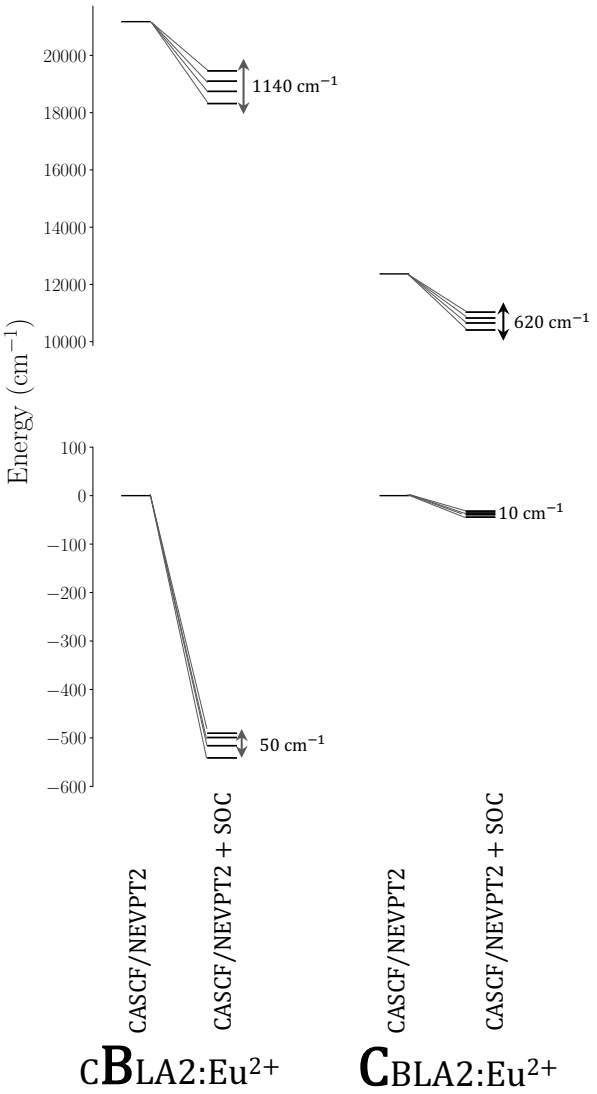

Figure S6b. SA-CASSCF(7,19)/NEVPT2 non-relativistic ground and lowest (emitting) excited state and their relaxation and splitting due SOC of the monomer structure of CBLA2:Eu^{2+} doped at Ba^{2+} and Ca^{2+} sites, respectively.

S III. Computational Protocol Summary

1) The lowest excitation energies, for all employed functionals, were converged at the trimer cluster size. In the case of the CBLA2 clusters the lowest excitation energy (optical BG) is observed for the clusters containing Ba^{2+} centers while in the case of RNLSO and RNLSO2 clusters the lowest excitation energy (optical BG) is observed for the clusters containing Na^{+} centers.

2) STEOM-DLPNO-CCSD showed as expected[25, 28] the best performance in computed experimental BGs of the host structures. In fact, the mean absolute errors (MAE) in the case of RNLSO and RNLSO2 drop below 0.03 eV in comparison to the available experimental data.

In contrast the employed TD-DFT functionals showed larger deviations as the computed MAE values decrease in the sequence PBE, PBE0, CAM-B3LYP, B2PLYP and ωB2PLYP (MAE=4.6, 3.1, 2.4, 3.0, and 1.9 eV, respectively). This is due to the fact that the probed state reflects a non-rigid $O^{2-} - 2p \rightarrow Na^{+} - 3s$ (for RNLSO and RNLSO2) and $N^{3-} - 2p \rightarrow Ba^{2+} - 5d$ (for CBLA2) ligand to metal charge transfer (LMCT) transitions. For RNLSO this is collectively shown in Figure S4.

3) In sharp contrast, with the BG energy computations on the undoped phosphors, TD-DFT performed better when employed to compute the 1st excitations energies of the Eu^{2+} doped structures in particular the hybrid functionals (PBE0, CAM-B3LYP) show noticeable smaller deviations when compared against the SA-CASSCF(7,19)/NEVPT2 computed values, MAE ~ 500-700 cm^{-1} (0.06-0.09 eV). This is due to the different nature of the probed transition. In the case of the undoped phosphors the transitions that dominate the BG energies are of LMCT character while in the case of the Eu^{2+}-doped ones they have a rigid $4f \rightarrow 5d$ character.

4) In an effort to investigate the influence of spin-orbit coupling SOC effects in the emissive states of $4f^{6}5d^{1}$ excited configuration, preliminary results on the CBLA2 cuboids (Figure S6b) showed that at the relativistic limit the $4f^{6}5d^{1}$ multiplet splits by about ~600-1100 cm^{-1} which is consistent with the atomic Eu^{2+} SOC constant (1200 cm^{-1} calculated employing ab initio ligand field theory[30-33] ($4f^{6}5d^{1}$)). While this state splitting can influence the magnetic nature of the emissive multiplet and fine tune the narrow band width has only limited impact to the emissive band energy position. Hence, in this study SOC effects were excluded from the computational calculations.

5) Based on the analysis so far one would conclude that a natural choice for investigating the emission mechanism of Eu^{2+} doped phosphors bearing multiple candidate doping centers would be to resort on wavefunction based theories like SA-CASSCF/NEVPT2. Nevertheless owning to the rigid nature of the emissive states in these and the fact that SOC effects are not influencing effectively the energy position of the involved absorption and emission spectra we investigate the possibility of employing TD-DFT level of theories in lines with previous studies on Eu^{2+}-doped phosphors.[28]

6) Based on its performance the PBE0 hybrid functional was employed to compute the absorption spectra of the study set of the Eu^{2+}-doped phosphors in the sequence monomer to pentamer clusters. The results are presented in Figure S5 showing once again that in all studied cases the TD-DFT/PBE0 computed spectra converge for the trimer cluster size. Provided that the spectra are shifted by $\sim 500 - 700$ cm^{-1}, the computed spectra are also in satisfactory visual agreement to experiment in terms of the number and the relative intensities of the computed bands. Hence in the following sections the trimer structures are chosen for the production calculations and analysis of the absorption and emission processes employing the TD-DFT/PBE0 computational protocol in conjunction with the excited state dynamics (ESD).

S IV. Insights into Eu^{2+} doping

1. Definition of the Doping energy in the framework of DLPNO-CCSD(T) level of theory

In this concept the doping energy $\Delta E_{Doping}^{CCSD(T)}$ as difference between binding energy in the Eu-doped and the host structure and is computed according to equation (1)

$$\begin{aligned}\Delta E_{Doping}^{CCSD(T)} &= \Delta E_{Doped-str.}^{CCSD(T)} - \delta\ \Delta E_{Host}^{CCSD(T)} \\ &= \left[E_{Doped-Str.}^{CCSD(T)} - E_{Ligand}^{CCSD(T)} - E_{free-Eu^{2+}}^{CCSD(T)} \right] \\ &\quad - \delta \left[E_{Host}^{CCSD(T)} - E_{Ligand}^{CCSD(T)} - E_{free-M^{m+}}^{CCSD(T)} \right]\end{aligned} \tag{1}$$

where $\Delta E_{Doped-str.}^{CCSD(T)}$, $\Delta E_{Host}^{CCSD(T)}$ are total interaction in doped and host (undoped) structures, respectively. They are expressed in terms of the following energy quantities; 1) the energy of embedded Eu^{2+}-doped structure ($E_{Doped-Str.}^{CCSD(T)}$), 2) the energy of the embedded host structure ($E_{Host}^{CCSD(T)}$), 3) the energy of the embedded host structure without the M^{m+} ion ($E_{Ligand}^{CCSD(T)}$), 4) the energy of the free Eu^{2+} ($E_{free-Eu^{2+}}^{CCSD(T)}$) and 5) the energy of the free M^{m+} ions ($E_{free-M^{m+}}^{CCSD(T)}$). δ , is a coefficient introduced to compensate charge change during Eu^{2+} doping and equals $(charge_{Eu^{2+}} - charge_{M^{m+}} + 1)$, giving $\delta = 1$ for Ca^{2+}/Ba^{2+} and 2 for Na^{+}/Rb^{+}.

2. Understanding the Eu^{2+} doping in the framework of DLPNO-CCSD(T)/LED analysis

Entering the local energy decomposition (LED) analysis, the DLPNO-CCSD(T) computed doping energies are decomposed into a set of chemically and physically meaningful inter- and intra-fragment contributions between the Eu^{2+} doped center and the host cuboid environment. This analysis is used below in an effort to shed light on 1) the type of interactions

encountered by Eu^{2+} per doping site and 2) the favorable doping scheme that is followed by each phosphor in the study set.

As is presented with black bars in Figure S7, in the framework of local energy decomposition (LED), the doping energy ($\Delta E_{Doping}^{CCSD(T)}$), for all studied systems at different probable Eu^{2+} doping centers, are calculated as the difference in binding energy (ΔE_{int}) between Eu^{2+}-doped structure and host, taking into account charge compensation coefficient (δ) as following Equation (1). (ΔE_{int}) in each structure is decomposed in reference DFT/PBE0 contributions (ΔE_{int}^{REF}) and correlation contributions (ΔE_{int}^{C}) and reads as follows in relation (2)

$$\Delta E_{int} = \Delta E_{int}^{REF} + \Delta E_{int}^{C} \quad (2)$$

ΔE_{int}^{REF} and ΔE_{int}^{C} are, in principle, representing the ionic and covalent interaction, respectively.

$$\Delta E_{int}^{REF} = \Delta E_{El-prep.}^{REF(PBE0)} + \Delta E_{Elstat.}^{REF(PBE0)} + \Delta E_{Exch.}^{REF(PBE0)} \quad (3)$$

ΔE_{int}^{REF} is the sum of three contributions, the electronic preparation, the electrostatic and the exchange interactions, as shown in relation (3), based on KS orbitals and QROs for host and doped structures, respectively.

$\Delta E_{Elstat.}^{REF(PBE0)}$ *and* $\Delta E_{Exch.}^{REF(PBE0)}$ represent the permanent and induced electrostatic and exchange interactions between the electron densities of the deformed fragments. The electronic preparation $\Delta E_{El-prep.}^{REF(PBE0)}$ represents the energy necessary to distort the individual electron densities of the fragments from their free state to their current state in the doped system, that is encounter to the commonly known "Pauli repulsion" and the polarization effects.[34]

ΔE_{int}^{C} is the sum of, DLPNO-CCSD(T) correlations, divided into contributions of the strong pairs $\left(\Delta E_{int}^{C-\mathrm{SP}}\right)$, weak pairs $\left(\Delta E_{int}^{C-\mathrm{WP}}\right)$, and triples correction $\left(\Delta E_{int}^{C-(T)}\right)$ in the interaction as shown in relation (4).

$$\Delta E_{int}^{C} = \Delta E_{int}^{C-\mathrm{SP}} + \Delta E_{int}^{C-\mathrm{WP}} + \Delta E_{int}^{C-(T)} \quad (4)$$

The correlation interaction energy can be effectively decomposed dispersive $\left(\Delta E_{disp}^{C-CCSD}\right)$ and non-dispersive $\left(\Delta E_{non-disp}^{C-CCSD}\right)$ correlation contributions as shown in relation (5).

$$\Delta E_{int}^{C} = \Delta E_{disp}^{C-CCSD} + \Delta E_{non-disp}^{C-CCSD} \quad (5)$$

In principle ΔE_{int}^{REF} is associated with the stable formation of the Eu^{2+}-doped phosphor and it is sensitive to the interactions with the first and second coordinations spheres of the host cuboid structures. Hence repulsive or positive ΔE_{int}^{REF} interactions translate to an unrelaxed EuL_8 formations while negative or attractive ΔE_{int}^{REF} interactions translate to a rather relaxed and thus stable EuL_8 cuboid formation. As has been discussed to a certain extend relaxed/unrelaxed EuL_8 cuboid formations may associate to the magnitude of the Stokes shifts.[35] In practice as has been discussed[28] and will be also shown below such relations require a proper treatment of the luminescence process. Similarly, to ΔE_{int}^{REF}, ΔE_{int}^{C} is sensitive to the formation of the bonding character around the EuL_8 cuboids.

Table S4. Eu^{2+} doping energies for CBLA2, CBLA, RNLSO, and RNLSO2, at the different candidate doping centers of trimers clusters computed at DFT(PBE0) and DLPNO-CCSD(T) methods.

Phosphor	Doping site	Doping Energy (eV)	
		PBE0	DLPNO-CCSD(T)
$CaBa[LiAl_3O_4]_2:Eu^{2+}$ CBLA2	Ba^{2+}	-1.62	-3.67
	Ca^{2+}	1.65	-0.67
$Ca_3Ba[LiAl_3O_4]_4:Eu^{2+}$ CBLA	Ba^{2+}	-2.93	-3.12
	$Ca(1)^{2+}$	0.63	-2.81
	$Ca(2)^{2+}$	1.33	-1.97
$RbNa_3[Li_3SiO_4]_4:Eu^{2+}$ RNLSO	$Na(1)^{+}$	-2.55	-1.32
	$Na(2)^{+}$	-2.09	-0.88
	Rb^{+}	-4.42	-1.66
$RbNa[Li_3SiO_4]_2:Eu^{2+}$ RNLSO2	Na^{+}	-2.14	-0.87
	Rb^{+}	-4.51	-3.34

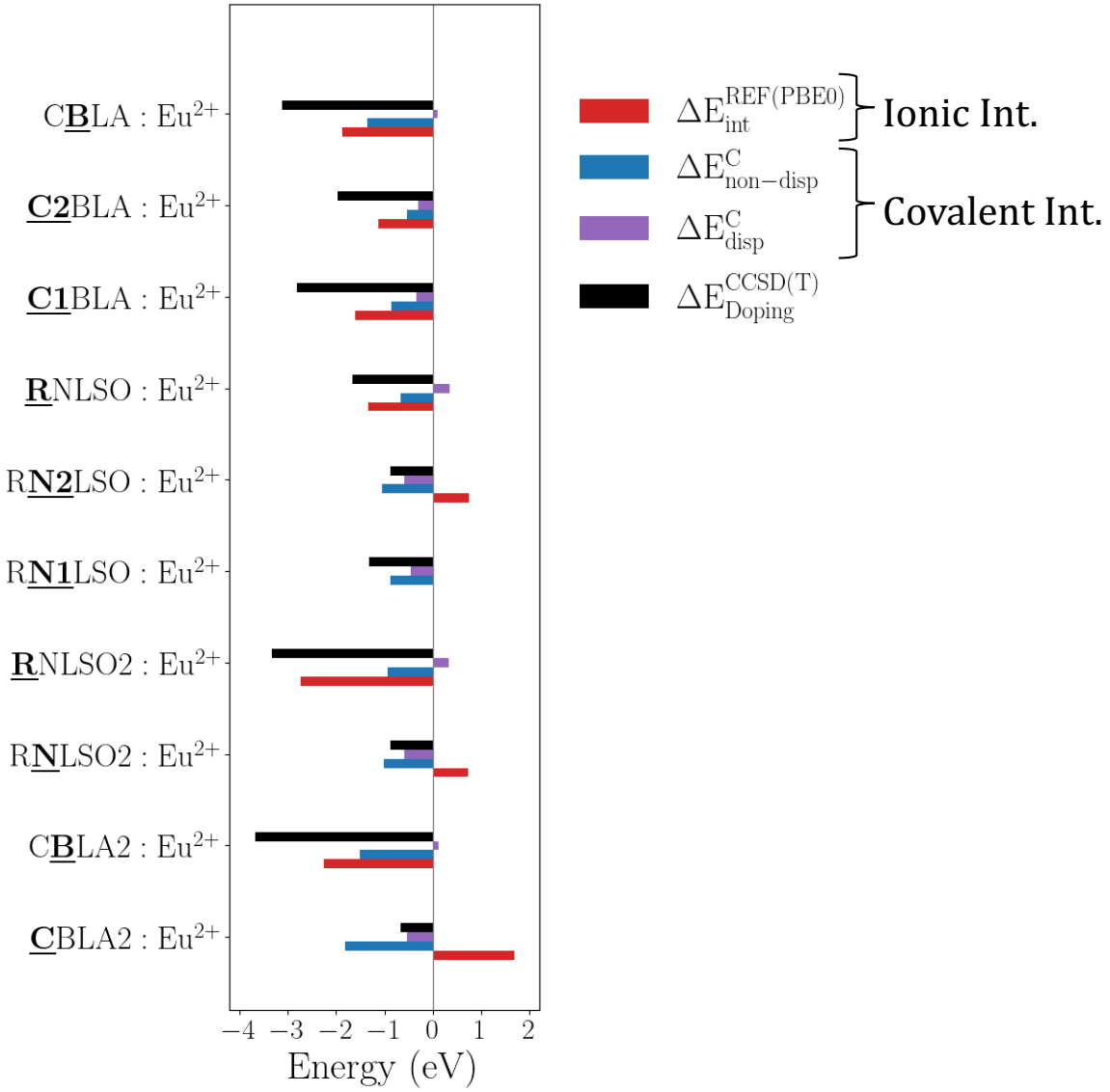

Figure S7. Local energy decomposition (LED) analysis of DLPNO-CCSD(T) doping energies (black bars) for for all the studied systems (CBLA2, RNLSO2, RNLSO and proposed CBLA) at the all probable sites for Eu^{2+} doping in terms of ionic (ΔE_{int}^{REF}) and covalent ($\Delta E_{non-disp}^{C}$ and ΔE_{disp}^{C}) interactions, shown in in red, blue, and purple bars, respectively.

3. Electronic Structure Analysis. Insights into the Emission mechanism of multiple doping centers

The electronic structure principles that determine the emission properties of Eu^{2+}-doped phosphors have been recently discussed in detail.[28] Here, we will briefly recapitulate them and expand the discussion to cover multiple doping centers. The free Eu^{2+} ion has a very stable octet ground state with a half-filled f-shell (GS) $^8S_{7/2}$ ($4f^75d^0$). The lowest excited state of the free ion arises from a localized spin-flip excitation to give a $^6P_{7/2}$ ($4f^75d^0$) multiplet state. This transition is however, both parity and spin forbidden and difficult to reach ~3.8 eV from the GS ($^8S_{7/2}$)[36], in addition it is effectively not tunable by the coordination environment effects due to the strong shielding of $4f^7$ electrons by the outer ($6p^6$ and $6s^2$) fully occupied orbital shells. The other and more interesting excitation pathway is to excite an electron to the empty 5d orbitals via spin-conserving one-electron excitations $^8S_{7/2}$ ($4f^7$) $\longrightarrow {}^7F \otimes {}^2D$ ($4f^65d^1$). While these transitions are located at somewhat high energies, (e.g. the atomic spectroscopic ^8H term ($4f^65d^1$) is located at about 4.2 eV), they are both parity and spin allowed. Hence, these are intense transitions that are highly tunable by the environment given the strong interaction of the outer 5d-orbital shell with the ligand framework.

When Eu^{2+} is doped in 8-fold coordinated host environments, in accord with Hund's rule the interelectronic repulsion stabilizes the highest multiplicity (2S+1=8) excited state multiplets of the $4f^65d^1$ configuration over the 2S+1=8 $4f^75d^0$ ground state multiplets. In addition, the cubic ligand field splitting will lift the degeneracy of the 4f and 5d orbitals in an inverted octahedral order ($\Delta_{cubic} = -8/9\Delta_{Oh}$) leading to a ground state electron configuration: $\underbrace{t_{2u}^3\ t_{1u}^3\ a_{2u}^1}_{4f^7}\ \underbrace{e_g^0 t_{2g}^0}_{5d^0}$ of the ($4f^75d^0$) shells. Further distortions towards tetragonal/trigonal ligand fields will lift any remaining orbital degeneracies and consequently the ground and excited state degeneracies. As has been explored in detail,[28] quantities like the ligand field splitting, band gap energies and Stokes shifts are important quantities of the absorption and emission processes as they can be employed to determine the energy position and the bandwidth of the different spectral features. Within the 1-electron picture these quantities can be collectively represented by the ligand field splitting ΔE_{LF} and the f-d energy separation ΔE_{fd} and Stokes shift ΔE_S. As shown in Figure 1, across the study set a collection of $Eu(N/O)_8$ cuboids may form at the various doping positions. All the cuboids are distorted from the ideal cubic symmetry which significantly affects the nature of the involved absorption and emission processes.

While CBLA2 and RNLSO2 are isotypic (Figure 1) the C_{2h} symmetric BaN_8 and CaN_8 cuboids deviate by only 1-2% from the 'ideal' D_{4h} symmetry. Hence in a first approximation the Eu^{2+} doping is discussed considering D_{4h} symmetric EuN_8 cuboids. In this view doping at Ba^{2+} center forms a tetragonally elongated (D_{4h}) EuN_8 cuboid. This leads to absorption and emission processes consisting from the z-polarized dipole allowed $\mathrm{Eu}\ 4f_{z3} \leftrightarrow \mathrm{Eu}\ 5d_{z2}$ electron transitions and decays. In contrast, doping at Ca^{2+} center leads to a strongly tetragonally compressed (D_{4h}) EuN_8 cuboid. As shown in Table 1, in comparison to the tetragonally elongated cuboids the ΔE_{LF} is increased while the ΔE_{fd} is decreased rather strongly leading to red-shifted absorption and emission processes consisting from the dipole forbidden $\mathrm{Eu}\ 4f_{xyz} \leftrightarrow \mathrm{Eu}\ 5d_{x2-y2}$ electron transitions and decays. This is not surprising as in fact the color of the phosphors is associated by the predominant $\mathrm{Eu} - 4f \leftrightarrow \mathrm{Eu} - 5d$ transition.[28] Symmetry reduction towards C_{2h} symmetric EuN_8 cuboids (Figure S8b) will render the $\mathrm{Eu}\ 4f_{xyz} \leftrightarrow \mathrm{Eu}\ 5d_{x2-y2}$ electron decay a dipole allowed process.

A similar picture is observed in the case of RNLSO:Eu^{2+} and RNLSO2:Eu^{2+} when Eu^{2+} is doped at Rb^+ and $Na(1)^+/Na^+$ positions. In particular, doping at Rb^+ positions forms tetragonally elongated (C_{2h}) EuO_8 cuboids. This leads to absorption and emission processes consisting from the z-polarized dipole allowed $\mathrm{Eu}\ 4f_{z3} \leftrightarrow \mathrm{Eu}\ 5d_{z2}$ electron transitions and decays. In contrast, doping at $Na(1)^+/Na^+$ positions leads to tetragonally compressed (C_{2h}) EuO_8 cuboids. Once again in comparison to the elongated EuO_8 cuboids the ΔE_{LF} is increased while the ΔE_{fd} is decreased leading to red-shifted absorption and emission processes consisting from dipole allowed $\mathrm{Eu}\ 4f_{xyz} \leftrightarrow \mathrm{Eu}\ 5d_{x2-y2}$ electron transitions and decays. In the case of RNLSO:Eu^{2+} when Eu^{2+} is doped at $Na(2)^+$ position a tetragonally compressed (D_{2d}) EuO_8 cuboid is formed. In comparison to the tetragonally compressed (C_{2h}) EuO_8 cuboids when Eu^{2+} doping occurs at the $Na(1)^+$ positions the ΔE_{LF} and ΔE_{fd} are further increased and decreased, respectively. As a result, further red-shifted absorption and emission processes are observed which consist however of dipole forbidden $\mathrm{Eu}\ 4f_{xyz} \leftrightarrow \mathrm{Eu}\ 5d_{x2-y2}$ electron transitions and decays (Figure S8).

Qualitatively, the above analysis suggests that the blue-shifted main intensity band as well as the red-shifted low intensity band of CBLA2:Eu^{2+} originates from Eu^{2+} doping at Ba^{2+} and Ca^{2+} position, respectively. Similarly, in the case of RNLSO:Eu^{2+} and RNLSO2:Eu^{2+} emissions are expected to increase in energy in the sequence of the $Na(2)^+$, $Na(1)^+$ and Rb^+ doping positions. Among them the $Na(2)^+$ positions are the least probable as they are associated with dipole forbidden transitions.

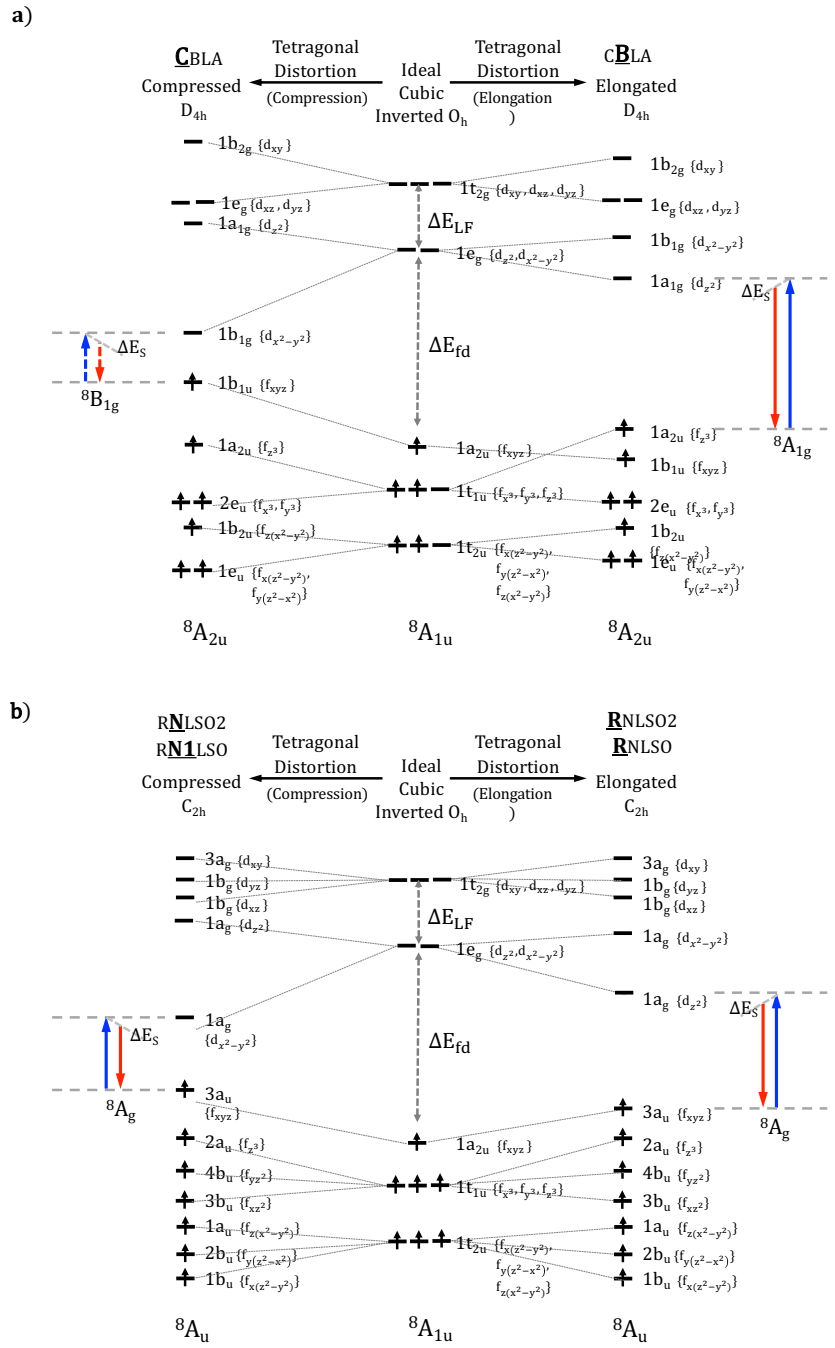

Figure S8. Molecular orbital diagram of the case of the study set of phosphors in which the Eu^{2+} doped centers at the Ca^{2+}, Ba^{2+}, $Na(1)^{+}/Na^{+}$ or Rb^{+} form $Eu(N/O)_8$ cuboids of distorted cubic coordination environments a) D_{4h} for CBLA2:Eu^{2+}, CBLA:Eu^{2+} and b) C_{2h} for RNLSO:Eu^{2+} and RNLSO2:Eu^{2+}. The involved electronic transitions consisting the absorption and emission processes are adopted with the 1-electron picture. Blue and red arrows indicate the most important absorption and relevant emission processes, respectively. Dotted arrows indicate dipole forbidden transitions. ΔE_{LF}, ΔE_{fd} and ΔE_S, represent the ligand field splitting of Eu 5d, the energy separation between barycenter's of Eu 4f-5d manifolds, and the expected

Stokes shift, respectively. In the abbreviated name of phosphor, the doped site is underlined and in bold font.

In the case of RNLSO, (Figure S9 d) the main absorption band located at 20000 and 30000 cm^{-1} spectrum window contains contributions from Eu^{2+} center doped at both $Na(2)^{+}$ (band 1, 2), $Na(1)^{+}$ (band 3) and Rb^{+} (band 4) centers. Similarly, the high energy absorption band located at 32000 and 43000 cm^{-1} spectrum window contains mixed contributions from Eu^{2+} centers doped at both and Rb^{+} (band 5), $Na(1)^{+}$ (band 6) and $Na(2)^{+}$ (band 7) centers. Analysis shows that the main emission band arises from an Eu^{2+} center doped at the $Na(1)^{+}$ site and takes place from the non-bonding Eu $5d_{x^2-y^2}$ based MO with a^2 of 0.95 reached by absorption band 3. On the contrary, the lower energy and weak intensity emission band arises from an Eu^{2+} center doped at the $Na(2)^{+}$ site involving a Eu $5d_{x2-y2}$ based molecular orbital MO with covalency factor a^2=0.87 reached by absorption band 1. Interestingly, although Rb^{+} site showed the highest probability for Eu^{2+} doping, it has no contribution in the emission process because its lowest excited state lies beyond the employed experimental laser, band 4. Hence assuming direct 1-photon optical conditions the relevant states reached by the absorption process are not populated. It should be emphasized that optical re-absorption of light and/or energy transfer processes might further influence the spectral intensities. This is beyond the scope of the current study.

In the case of RNLSO2 (Figure S9 b), the main absorption band located at 18000 and 32000 cm^{-1} spectrum window contains contributions from Eu^{2+} center doped at both Na^{+} (bands 1, 3), and Rb^{+} (bands 2, 4) centers. The high energy shoulder located at 37000 cm^{-1} arises from Eu^{2+} centers doped at Na^{+} (band 5) centers. Analysis shows that the main emission band 1* arises from an Eu^{2+} centers doped at the Na^{+} sites and takes place from the non-bonding Eu $5d_{x^2-y^2}$ based MO with a^2 of 0.92 leading to broader emission than in the case of RNLSO. A weak blue shifted emission band 2* arises from an Eu^{2+} centers doped at the Rb^{+} sites reached by absorption band 2 and takes place from the non-bonding Eu $5d_{z2}$ based MO with a^2 = 0.97. In accord with the experiment, as shown in Figure S10, by bringing the absorption

laser in resonance with absorption band 2 corresponding to Eu^{2+} centers doped at the Rb^{+} sites it is possible to tune the emission intensities of band 1* and band 2*.

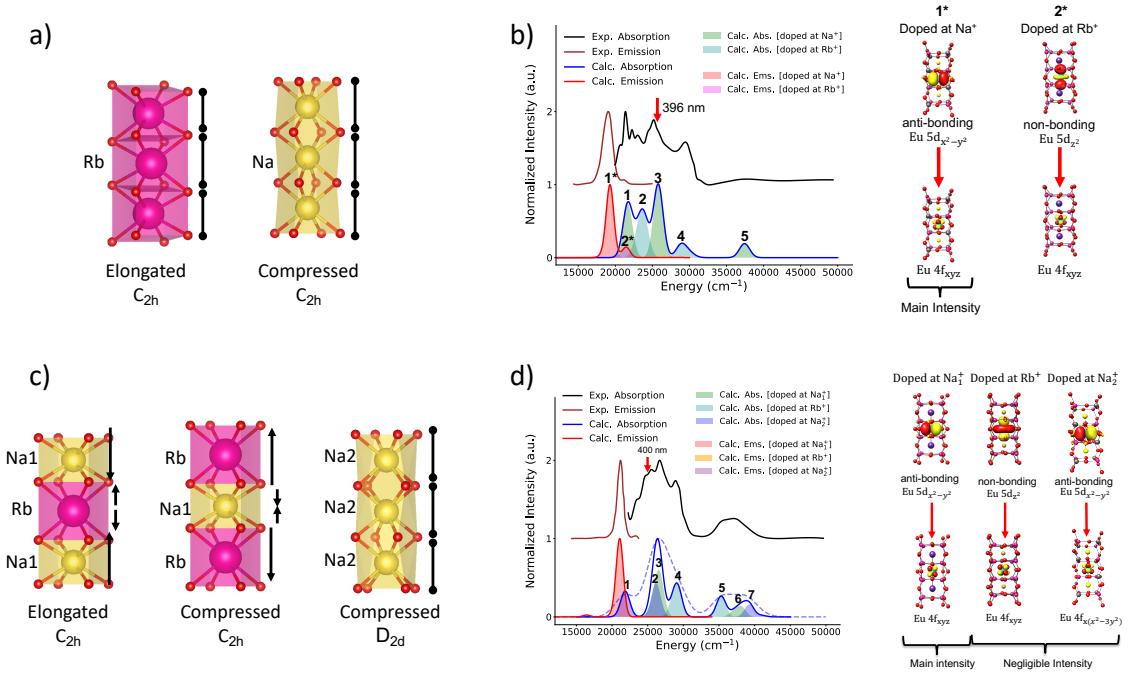

Figure S9. a, c) Trimer cuboids and b,d) experimental and ESD/TD-DFT/PBE0 calculation absorption and emission spectra alongside NTO analysis of the lowest excited states at probable doping sites for RNLSO2:Eu^{2+} and RNLSO:Eu^{2+}, respectively.

As shown in Figure S9, the emission in RNLSO2 at Na^{+} is broader compared to RNLSO at $Na(1)^{+}$ due to the nature of the non-bonding Eu $5d_{x^2-y^2}$ based MO. Additionally, a weak blue-shifted emission band is observed in RNLSO2, originating from Eu^{2+} centers doped at the Rb^{+} sites. So, the transformation from RNLSO2 to RNLSO lead to improvement of the luminescence in the oxide domain, provide a valuable strategy to model new CBLA system to word optimization of the CBLA2 properties to achieve desired luminescent properties.

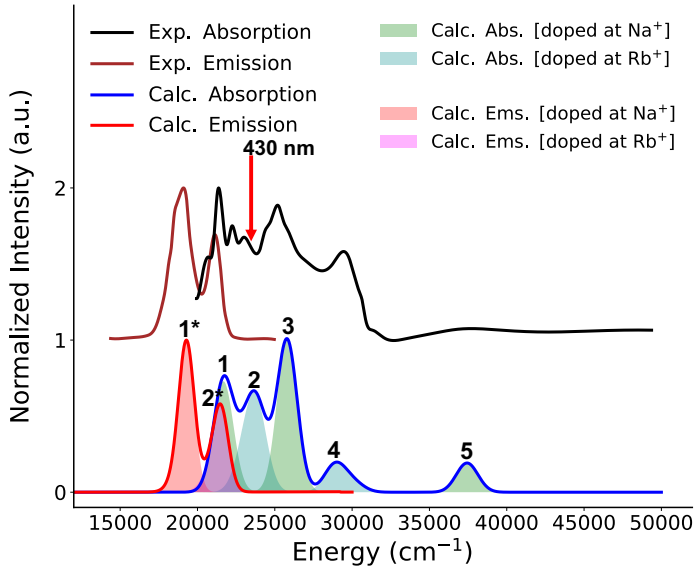

Figure S10. RNLSO2 experimental (black), calculated TD-DFT/PBE0 absorption (blue) spectra and experimental (brown), ESD/TD-DFT/PBE0 calculated (red) emission spectra. The emission spectrum is computed on the basis of a 430 nm laser that provides intensity enhancement to emission band 2* that originates from Eu^{2+}-doped at Rb^{+} centers.

S V. Descriptors Predicting Luminescence Properties of Solid-state Eu^{2+}-doped Phosphors

We have previously[28] defined general descriptors that are able to predict the emission color and bandwidth of Eu^{2+}-doped phosphors bearing a single candidate center for Eu^{2+} doping. These descriptors are based on the electronic characteristic of the first excited state dominating the emission process. In particular the emission band properties can be predicted from the energy position of the first excited state ($4f^6 5d^1$) and the covalency cofactor a^2 of the Eu 5d based MO. At the TD-DFT PBE0/def2-TZVP level of theory the corresponding linear relations read:

$$\text{Expected Emission Band Max}(\text{cm}^{-1}) = 0.9334 * \text{E}_1(\text{cm}^{-1}) - 419.04(\text{cm}^{-1}) \quad (1)$$

$$\text{Expected Emission Band FWHM}(\text{cm}^{-1}) = -2530.7 * \text{Eu 5d } a^2 + 3638.4(\text{cm}^{-1}) \quad (2)$$

where, E_1 is the energy position of the 1st absorption band, while the Eu 5d a^2 coefficient is degree of covalency in $\text{Eu(5d)} - \text{L(2p)}$ bond. As previously[28] described, Eu 5d a^2 coefficient is directly extracted from involved acceptor NTO consisting the absorption band.

In a last step of our analysis, we test the applicability of the above descriptors by considering in addition the study set of Eu^{2+}-doped phosphors bearing multiple candidate centers for Eu^{2+} doping. As seen in Table S5, in all the cases the employed relations are able to predict the energy position, the shape and the bandwidth of the absorption and emission spectra showing excellent agreement between theory and experiment. In fact, for the study set of Eu^{2+}-doped phosphors containing one or multiple doping centers the predicted emission energy positions, the respective bandwidth and Stokes shifts show mean absolute errors (MAE) with respect to experiment that vary in the range 0.01, 0.04 and 0.16, respectively.

Table S5. Experimental versus predicted maximum emission energy positions and bandwidths according to the descriptors relations (1) and (2) for a given computed maximum absorption band maximum and the respective covalency factor (5d α^2) and calculated Stokes Shift ΔS for previously studied (BMS, SMS, CLA, SALON, SLBO):Eu^{2+} and (RNLSO, RNLSO2, CBLA2, CBLA):Eu^{2+}-doped phosphors at emitting centers.

Phosphor	Doping site	Experimental Emission Band			Calculated First Absorption band		Predicted Emission Band		
		Energy (cm^{-1})	Width (cm^{-1})	ΔS (cm^{-1})	Energy (cm^{-1})	Eu^{2+} 5d α^2	Energy (cm^{-1})	Width (cm^{-1})	ΔS (cm^{-1})
$Ba[Mg_3SiN_4]:Eu^{2+}$ BMS	Ba^{2+}	14920	2015	3500	16000	0.64	14925	1950	2810
$Sr[Mg_3SiN_4]:Eu^{2+}$ SMS	Sr^{2+}	16250	1150	750	18200	0.97	16260	1150	950
$Ca[LiAl_3N_4]:Eu^{2+}$ CLA	Ca^{2+}	14980	1340	1000	16150	0.84	14970	1350	847
$Sr[LiAl_3N_4]:Eu^{2+}$ SLA	Sr^{2+}	15380	1140	800	17200	0.96	15384	1160	840
$Sr[Al_2Li_2O_2N_2]:Eu^{2+}$ SALON	Sr^{2+}	16300	1220	1100	18100	0.90	16286	1220	1150
$SrLi_2[Be_4O_6]:Eu^{2+}$ SLBO	Sr^{2+}	22000	1220	980	23800	0.95	21929	1170	750
$RbNa_3[Li_3SiO_4]_4:Eu^{2+}$ RNLSO	$Na(1)^{+}$	21231	1015	--	23087	0.95	21968	1234	1120
$RbNa[Li_3SiO_4]_2:Eu^{2+}$ RNLSO2	Na^{+}	19121	1465	--	20030	0.92	19367	1496	670
$CaBa[LiAl_3N_4]_2:Eu^{2+}$ CBLA2	Ba^{2+}	15674	1191	--	17100	0.94	15484	1259	1570
	Ca^{2+}	12658	1450	--	14400	0.87	12970	1436	1310
$Ca_3Ba[LiAl_3N_4]_4:Eu^{2+}$ CBLA	$Ca(1)^{2+}$	--	--	--	15642	0.91	14600	1220	1460

MAE(%)	0.01	0.04	0.16

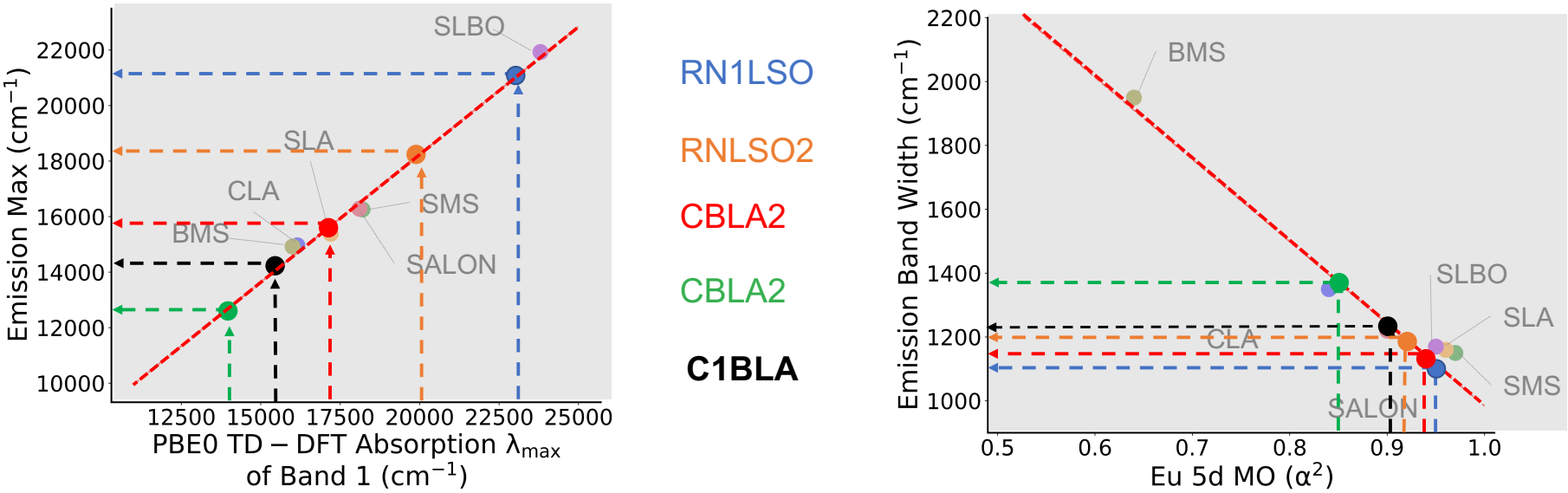

Figure S11. Using the previously defined descriptors to predict the luminescence band energy and bandwidth of the emitting centers of the studied (RNLSO:Eu^{2+} doped at $Na(1)^{+}$ in blue, RNLSO2:Eu^{2+} doped at Na^{+} in orange, and CBLA2:Eu^{2+} doped at Ba^{2+} in red and Ca^{2+} in green) and hypotetical CBLA:Eu^{2+} doped at $Ca(1)^{2+}$ in black.

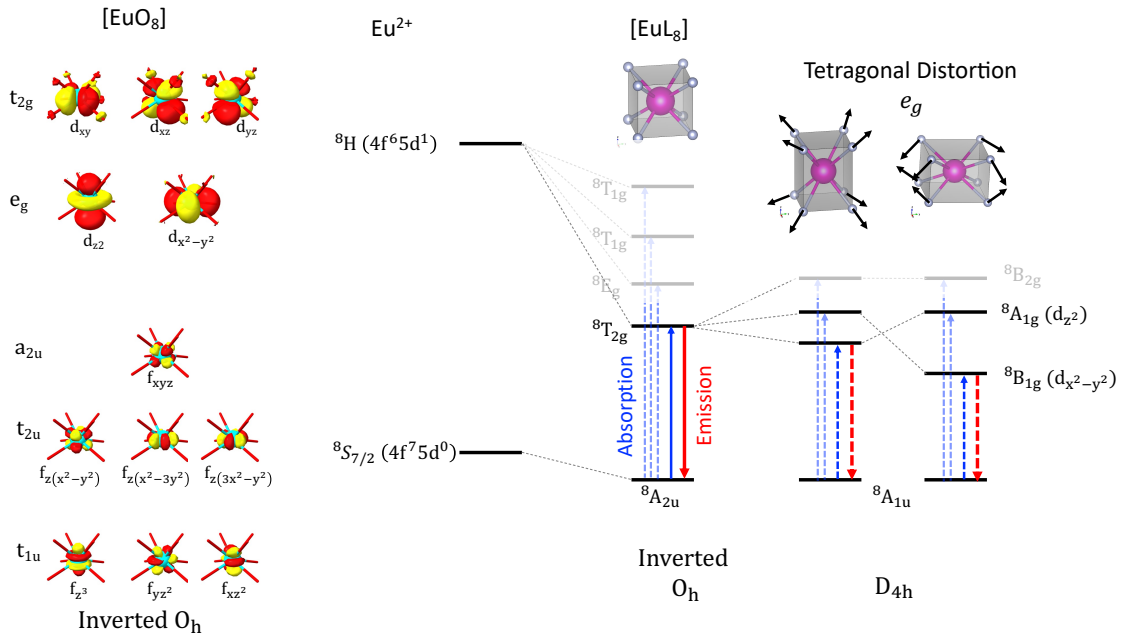

Figure S12. Molecular orbital diagram of the case of RNLSO:Eu^{2+} in which the Eu^{2+}-doped at the $Na(2)^{+}$ positions form D_{2d} tetragonally compressed EuO_8 cuboids. The involved electronic transitions consisting the absorption and emission processes are adopted with the 1-electron picture. Solid and blue arrows indicate the most important absorption processes. Red arrows indicate the relevant emission processes. Dotted arrows indicate dipole forbidden transitions.

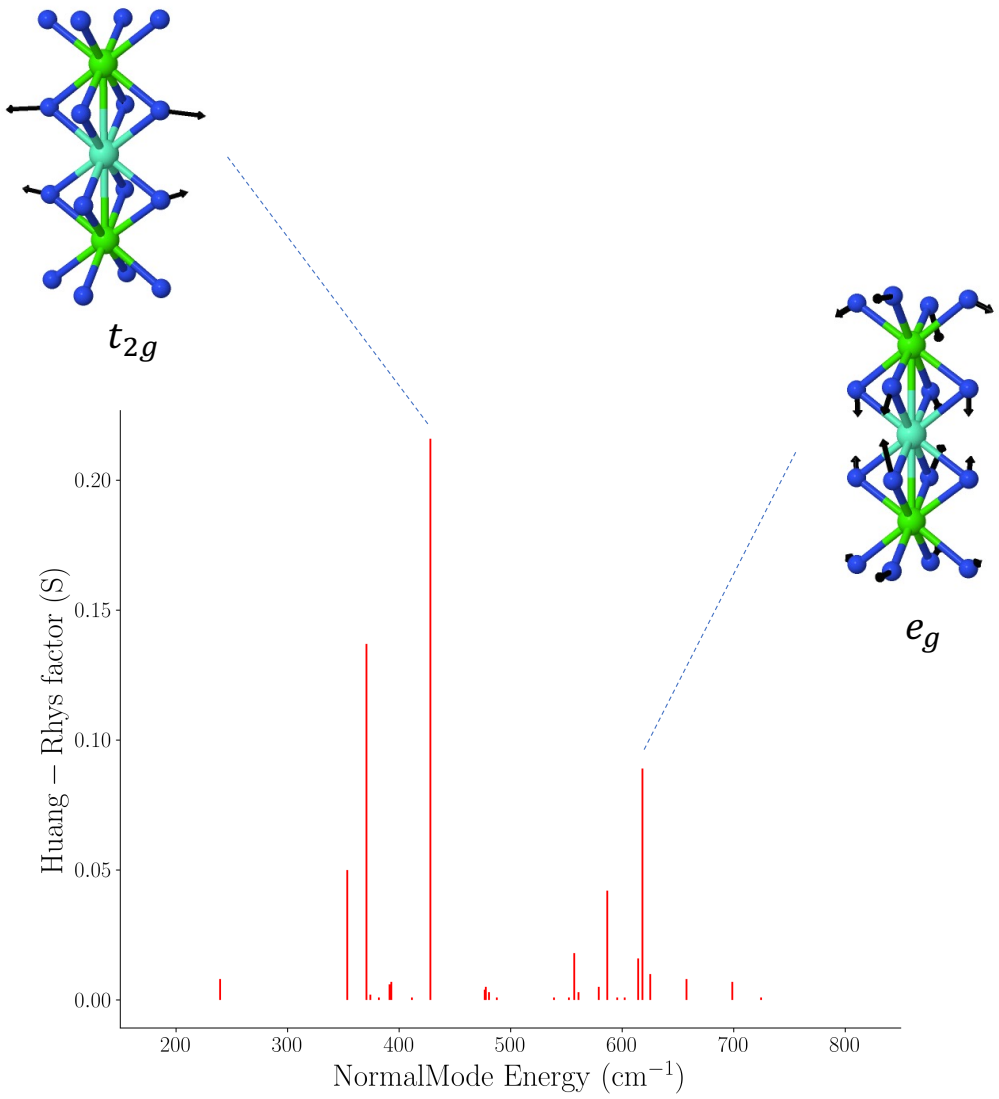

Figure S13. Huang-Rhys factors (S) distribution over the vibration degree of freedom of the emission transition in trimer model of CBLA2:Eu^{2+} doped at Ca^{2+} site. The highest contributing modes within the asymmetric and symmetric vibration regions (t_{2g} and e_g modes, respectively) are also visualized.

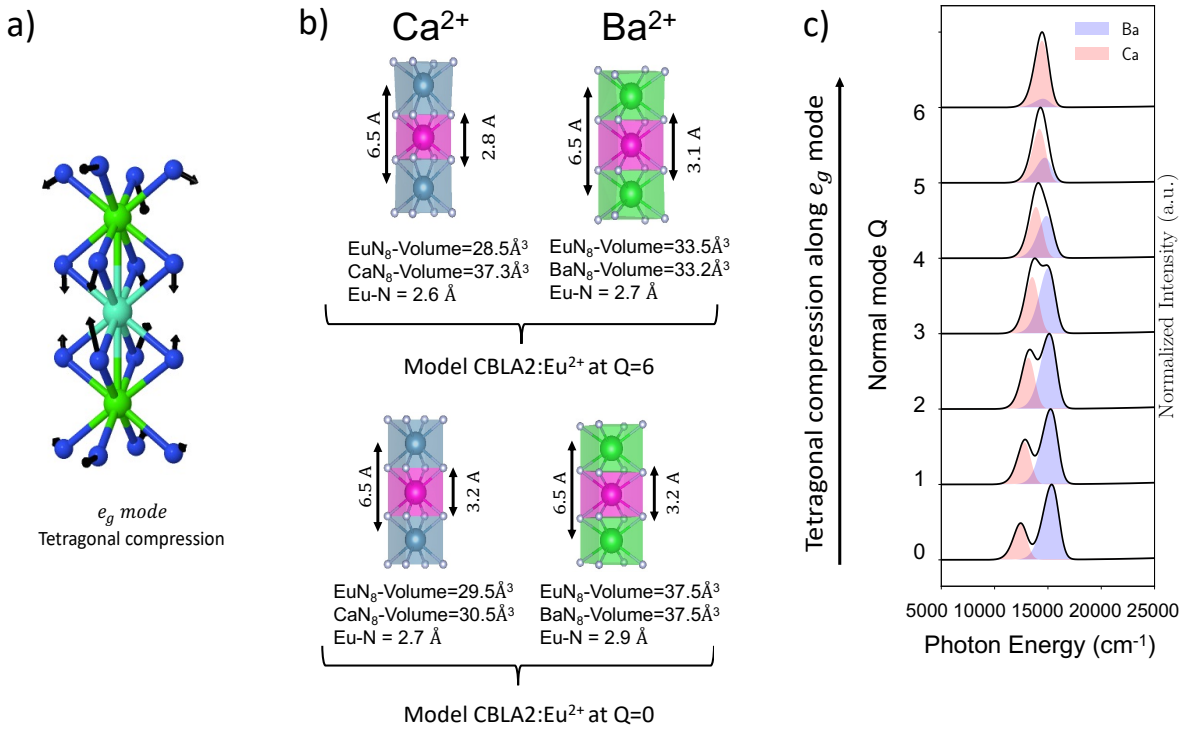

Figure S14. a) Illustration of the e_g vibrational mode leading the tetragonal compression pathway of the Eu^{2+} doped cuboids in CBLA2. b) The structures of the model CBLA2 along the tetragonal compresion pathway at the equilibrium (Q=0) and at selected point (Q=12). c) The normalized ESD/TDDFT/PBE0 computed emission spectra of the model CBLA2:Eu^{2+} along the tetragonal distortion pathway.

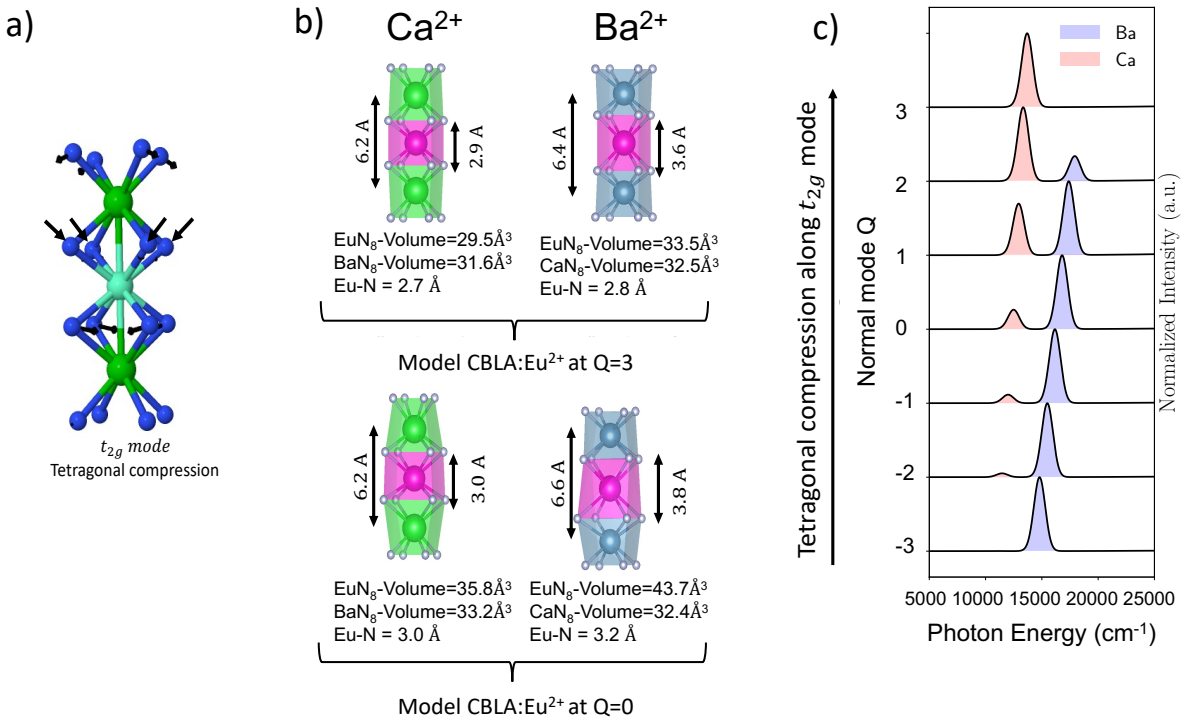

Figure S15. Illustration of the t_{2g} vibrational mode leading the tetragonal compression pathway of the Eu^{2+} doped cuboids in CBLA. b) The structures of the model CBLA along the tetragonal compresion pathway at the equilibrium (Q=0) and at selected point (Q=12). c) The normalized ESD/TDDFT/PBE0 computed emission spectra of the model CBLA:Eu^{2+} along the tetragonal distortion pathway.

S VI. Structural and optical properties of proposed CBLA:Eu^{2+} phosphor

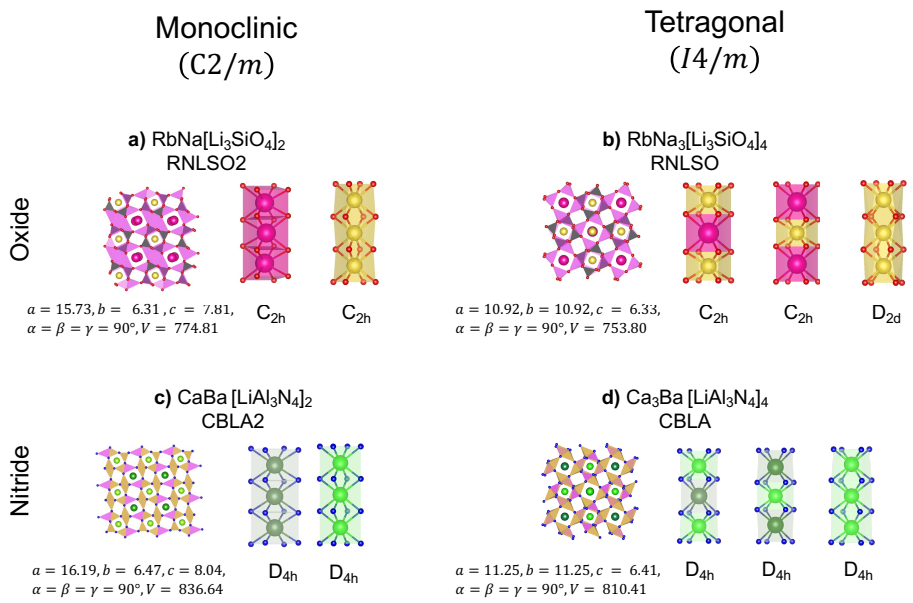

Figure S16. Space group, structural properties, and probable sites for Eu^{2+} doping for RNLSO2, RNLSO, CBLA2, and hypothetical CBLA Hosts.

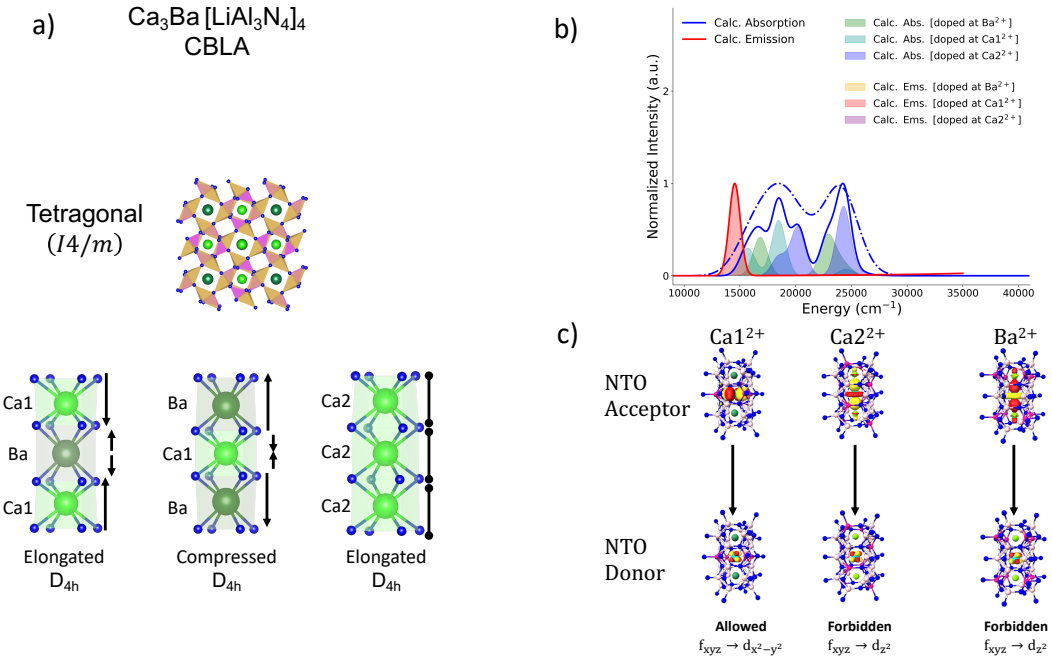

Figure S17. a) The crystalline structure optimized structure of CBLA and possible doping sites host ($Ca(1)^{2+}$, Ba^{2+} and $Ca(2)^{2+}$) and b) calculated TDDFT/PBE0 absorption (blue; solid and dashed lines plotted with gaussian broadening 1500, 3000 cm^{-1}, respectively) spectra and ESD/TDDFT/PBE0 calculated (red) emission spectra. Filled colored bands indicate individual contributions of the different Eu^{2+}-doped centers. c) The 1st transition responsible for emission upon relaxation for all the candidate Eu^{2+}-doped centers.

S VII.Examples of inputs for employed computational calculations

1. Charges convergence of ECPs and PCs (Ionic-Crystal-QMMM/DFT/PBE0)

```
! PBE0 def2-TZVP def2/J def2-TZVP/C PAL8
! RIJCOSX TightSCF defGrid3 NoTRAH CHelpG SOSCF
%MaxCore 5000

%SCF  MaxIter    500
      SOSCFStart 0.0001
      End

! Ionic-Crystal-QMMM
%QMMM Charge_Total     0
      ORCAFFFilename  "Na_3_RNLSO4_Na1_chg.ORCAFF.prms"
      QMAtoms         {0:10 15:26 39:46 59:74 161:168 } end
      HFLayerAtoms    {11:14 27:34 75:82 107:108 126:127 130:131 149 152:153 156 } end
      Charge_HFLayer   54
      HFLayerGTO      "LANL2DZ"
      HFLayerECP      "HayWadt"
      ECPLayers        2
      ECPLayerECP     "SDD"
      CONV_CHARGES             TRUE
      CONV_CHARGES_MAXNCYCLES  30
      CONV_CHARGES_CONVTHRESH  0.1
      ENFORCETOTALCHARGE       True
      PrintLevel               2
      End

* xyzfile  -53 1 Na_3_RNLSO4_Na1_chg.xyz
```

2. Optical band gap (TD-DFT/PBE0)

```
! PBE0 def2-TZVP def2/J def2-TZVP/C PAL8
! RIJCOSX TightSCF defGrid3 NoTRAH CHelpG
%MaxCore 5000

%SCF  MaxIter    500
      End

%TDDFT   NRoots    1
         MaxDim    10
         DoNTO     True
         End

! Ionic-Crystal-QMMM
%QMMM Charge_Total     0
      ORCAFFFilename  "Na_3_RNLSO4_Na1_chg.convCharges.ORCAFF.prms"
      QMAtoms         {0:10 15:26 39:46 59:74 161:168 } end
      HFLayerAtoms    {11:14 27:34 75:82 107:108 126:127 130:131 149 152:153 156 } end
      Charge_HFLayer   54
      HFLayerGTO      "LANL2DZ"
      HFLayerECP      "HayWadt"
      ECPLayers        2
      ECPLayerECP     "SDD"
      CONV_CHARGES             False
      ENFORCETOTALCHARGE       True
      PrintLevel               2
      End

* xyzfile  -53 1 Na_3_RNLSO4_Na1_chg.xyz
```

3. Optical band gap (STEOM-DLPNO-CCSD)

```
! RHF PBE0 def2-TZVP def2/J def2-TZVP/C PAL16
! RIJCOSX TightSCF defGrid3 NoTRAH CHelpG
! STEOM-DLPNO-CCSD TightPNO
%MaxCore 10000

%SCF  MaxIter    500
      End

%MDCI NRoots        1
      DTol        1e-4
      DLPNOLINEAR True
      NEWDOMAINS  True
      DoEOMMP2    True
      DoRECAN     True
      DoLeft      True
      DoTDM       True
      DoRootWise  True
      DoDbFilter  True
      MaxCore     10000
      MaxIter     500
      PrintLevel  3
      End

%TDDFT NROOTS    1
       MaxDim    10
       End

! MOREAD
%MOINP  "Na_3_RNLSO4_Na1_DLPNO_STEOM_CCSD.gbw_old"

! Ionic-Crystal-QMMM
%QMMM Charge_Total     0
      ORCAFFFilename  "Na_3_RNLSO4_Na1_chg.convCharges.ORCAFF.prms"
      QMAtoms         {0:10 15:26 39:46 59:74 161:168 } end
      HFLayerAtoms    {11:14 27:34 75:82 107:108 126:127 130:131 149 152:153 156 } end
      Charge_HFLayer   54
      HFLayerGTO      "LANL2DZ"
      HFLayerECP      "HayWadt"
      ECPLayers        2
      ECPLayerECP     "SDD"
      CONV_CHARGES             False
      ENFORCETOTALCHARGE       True
      PrintLevel               2
      End

* xyzfile  -53 1 Na_3_RNLSO4_Na1_chg.xyz
```

4. Doping energy (DLPNO-CCSD(T)) and LED

```
! RHF PBE0 def2-TZVP def2/J def2-TZVP/C PAL16
! RIJCOSX TightSCF defGrid3 NoTRAH CHelpG
! DLPNO-CCSD(T) TightPNO LED
%MaxCore 10000

%SCF  MaxIter    500
      End

%MDCI MaxIter       500
      LocMaxIter    500
      LocMaxIterLed       500
      TightPNOFragInter  {1 1} {2 2} {1 2}
      NormalPNOFragInter {1 3} {2 3}
      LoosePNOFragInter  {1 4} {1 5} {1 6} {2 4} {2 5} {2 6} {3 4} {3 5} {3 6} {4 5} {4 6} {5 6}
      MP2FragInter       {3 3}
      HFFragInter        {4 4} {5 5} {6 6}
      NoTriplesFragments  4, 5, 6
      End

! MORead
%MOInp "Na_3_RNLSO4_Na1_CCSDT.gbw_old"


! Ionic-Crystal-QMMM
%QMMM Charge_Total     0
      ORCAFFFilename  "Na_3_RNLSO4_Na1_chg.convCharges.ORCAFF.prms"
      QMAtoms         {0:10 15:26 39:46 59:74 161:168 } end
      HFLayerAtoms    {11:14 27:34 75:82 107:108 126:127 130:131 149 152:153 156 } end
      Charge_HFLayer   54
      HFLayerGTO      "LANL2DZ"
      HFLayerECP      "HayWadt"
      ECPLayers        2
      ECPLayerECP     "SDD"
      CONV_CHARGES             False
      ENFORCETOTALCHARGE       True
      PrintLevel               2
      End

* xyzfile  -53 1 Na_3_RNLSO4_Na1_chg.xyz

%GEOM Fragments
         1   { 0 }
             End
         2   { 1:8 }
             End
         3   { 15:22 }
             End
         4   { 9:10 23:26 39:46 59:74 161:168 }
             End
         5   { 11:14 27:34 75:82 107:108 126:127 130:131 149 152:153 156 }
             End
         End
      End
```

5. Absorption Spectra (TD-DFT/PBE0)

```
! PBE0 DKH2 DKH-def2-TZVP SARC/J def2-TZVP/C PAL8
! RIJCOSX SCFCONV10 DEFGRID3 CHELPG REDUCEDPOP UNO
%MaxCore 10000

%SCF  MaxIter    500
      End

%BASIS   NewGTO Eu "SARC-DKH-TZVPP" End
         NewGTO Rb "SARC-DKH-TZVPP" End
         End

%TDDFT   NRoots    25
         MaxDim    10
         DoNTO     True
         End

! Ionic-Crystal-QMMM
%QMMM Charge_Total     0
      ORCAFFFilename  "Eu_3_RNLSO4_Na1_chg.convCharges.ORCAFF.prms"
      QMAtoms         {0:10 15:26 39:46 59:74 161:168 } end
      HFLayerAtoms    {11:14 27:34 75:82 107:108 126:127 130:131 149 152:153 156 } end
      Charge_HFLayer   54
      HFLayerGTO      "LANL2DZ"
      HFLayerECP      "HayWadt"
      ECPLayers        2
      ECPLayerECP     "SDD"
      CONV_CHARGES             False
      ENFORCETOTALCHARGE       True
      PrintLevel               2
      End

* xyzfile  -52 8 Eu_3_RNLSO4_Na1_chg.xyz
```

6. Excited state dynamics and emission spectra (ESD/TDDFT/PBE0)

```
! PBE0 DKH2 DKH-def2-TZVP SARC/J def2-TZVP/C PAL16
! RIJCOSX SCFCONV10 DEFGRID3
%MaxCore 10000

%SCF  MaxIter    500
      End

%BASIS   NewGTO Eu "SARC-DKH-TZVPP" End
         NewGTO Rb "SARC-DKH-TZVPP" End
         End

%TDDFT   NROOTS      5
         MaxDim      10
         IROOT       1
         END

%ESD     ESDFLAG      FLUOR
         HESSFLAG     VGFC
         GSHESSIAN   "Eu_3_RNLSO4_Na1_RAMAN.hess"
         LINES        GAUSS
         INLINEW      500
         PRINTLEVEL   4
         DOHT         True
         End

! MORead
%MOInp "Eu_3_RNLSO4_Na1_TDDFT_PBE0.gbw"

! Ionic-Crystal-QMMM
%QMMM Charge_Total     0
      ORCAFFFilename  "Eu_3_RNLSO4_Na1_chg.convCharges.ORCAFF.prms"
      QMAtoms         {0:10 15:26 39:46 59:74 161:168 } end
      HFLayerAtoms    {11:14 27:34 75:82 107:108 126:127 130:131 149 152:153 156 } end
      Charge_HFLayer   54
      HFLayerGTO      "LANL2DZ"
      HFLayerECP      "HayWadt"
      ECPLayers        2
      ECPLayerECP     "SDD"
      CONV_CHARGES             False
      ENFORCETOTALCHARGE       True
      PrintLevel               2
      End

* xyzfile  -52 8 Eu_3_RNLSO4_Na1_chg.xyz
```

References

1. R. Dovesi, A. Erba, R. Orlando, C. M. Zicovich-Wilson, B. Civalleri, L. Maschio, M. Rérat, S. Casassa, J. Baima, S. Salustro and B. Kirtman, Quantum-mechanical condensed matter simulations with CRYSTAL, *WIREs Computational Molecular Science*, 2018, **8**, e1360.
2. A. Erba, J. K. Desmarais, S. Casassa, B. Civalleri, L. Donà, I. J. Bush, B. Searle, L. Maschio, L. Edith-Daga, A. Cossard, C. Ribaldone, E. Ascrizzi, N. L. Marana, J.-P. Flament and B. Kirtman, CRYSTAL23: A Program for Computational Solid State Physics and Chemistry, *J. Chem. Theory Comput.*, 2022, DOI: 10.1021/acs.jctc.2c00958.
3. W. R. Wadt and P. J. Hay, Ab initio effective core potentials for molecular calculations. Potentials for main group elements Na to Bi, *J. Chem. Phys.*, 1985, **82**, 284-298.
4. P. J. Hay and W. R. Wadt, Ab initio effective core potentials for molecular calculations. Potentials for the transition metal atoms Sc to Hg, *J. Chem. Phys.*, 1985, **82**, 270-283.
5. P. J. Hay and W. R. Wadt, Ab initio effective core potentials for molecular calculations. Potentials for K to Au including the outermost core orbitals, *J. Chem. Phys.*, 1985, **82**, 299-310.
6. T. H. Dunning and P. J. Hay, in *Methods of Electronic Structure Theory*, ed. H. F. Schaefer, Springer US, Boston, MA, 1977, DOI: 10.1007/978-1-4757-0887-5_1, ch. Chapter 1, pp. 1-27.
7. P. Fuentealba, H. Preuss and H. Stoll, A proper account of core-polarization with pseudopotentials: single valence-electron alkali compounds, *Chem. Phys. Lett.*, 1982, **89**, 418-422.
8. A. Bergner, M. Dolg, W. Küchle, H. Stoll and H. Preuß, Ab initio energy-adjusted pseudopotentials for elements of groups 13–17, *Mol. Phys.*, 1993, **80**, 1431-1441.
9. M. Kaupp, P. v. R. Schleyer, H. Stoll and H. Preuss, The question of bending of the alkaline earth dihalides MX2 (M= beryllium, magnesium, calcium, strontium, barium; X= fluorine, chlorine, bromine, iodine). An ab initio pseudopotential study, *J. Am. Chem. Soc.*, 1991, **113**, 6012-6020.
10. T. Leininger, A. Nicklass, W. Küchle, H. Stoll, M. Dolg and A. Bergner, The accuracy of the pseudopotential approximation: Non-frozen-core effects for spectroscopic constants of alkali fluorides XF (X= K, Rb, Cs), *Chem. Phys. Lett.*, 1996, **255**, 274-280.
11. S. Cox and D. Williams, Representation of the molecular electrostatic potential by a net atomic charge model, *J. Comput. Chem.*, 1981, **2**, 304-323.
12. K. B. Wiberg and P. R. Rablen, Comparison of atomic charges derived via different procedures, *J. Comput. Chem.*, 1993, **14**, 1504-1518.
13. D. Maganas, M. Roemelt, M. Havecker, A. Trunschke, A. Knop-Gericke, R. Schlogl and F. Neese, First principles calculations of the structure and V L-edge X-ray absorption spectra of V_2O_5 using local pair natural orbital coupled cluster theory and spin-orbit coupled configuration interaction approaches, *Phys. Chem. Chem. Phys.*, 2013, **15**, 7260-7276.
14. O. Demel, J. Pittner and F. Neese, A Local Pair Natural Orbital-Based Multireference Mukherjee's Coupled Cluster Method, *J Chem Theory Comput*, 2015, **11**, 3104-3114.
15. D. G. Liakos and F. Neese, Domain Based Pair Natural Orbital Coupled Cluster Studies on Linear and Folded Alkane Chains, *J Chem Theory Comput*, 2015, **11**, 2137-2143.
16. A. Dreuw and M. Head-Gordon, Single-reference ab initio methods for the calculation of excited states of large molecules, *Chem. Rev.*, 2005, **105**, 4009-4037.

17. J. P. Perdew, K. Burke and Y. Wang, Generalized gradient approximation for the exchange-correlation hole of a many-electron system, *Phys. Rev. B: Condens. Matter*, 1996, **54**, 16533.
18. C. Adamo and V. Barone, Toward reliable density functional methods without adjustable parameters: The PBE0 model, *J. Chem. Phys.*, 1999, **110**, 6158-6170.
19. J. P. Perdew, M. Ernzerhof and K. Burke, Rationale for mixing exact exchange with density functional approximations, *J. Chem. Phys.*, 1996, **105**, 9982-9985.
20. J. P. Perdew, K. Burke and M. Ernzerhof, Generalized Gradient Approximation Made Simple, *Phys Rev Lett*, 1996, **77**, 3865.
21. T. Yanai, D. P. Tew and N. C. Handy, A new hybrid exchange–correlation functional using the Coulomb-attenuating method (CAM-B3LYP), *Chem. Phys. Lett.*, 2004, **393**, 51-57.
22. S. Grimme, Semiempirical hybrid density functional with perturbative second-order correlation, *J. Chem. Phys.*, 2006, **124**, 034108.
23. M. Casanova-Páez, M. B. Dardis and L. Goerigk, ωB2PLYP and ωB2GPPLYP: The First Two Double-Hybrid Density Functionals with Long-Range Correction Optimized for Excitation Energies, *J. Chem. Theory Comput.*, 2019, **15**, 4735-4744.
24. L. M. J. Huntington, M. Krupička, F. Neese and R. Izsák, Similarity transformed equation of motion coupled-cluster theory based on an unrestricted Hartree-Fock reference for applications to high-spin open-shell systems, *J. Chem. Phys.*, 2017, **147**, 174104.
25. A. Dittmer, R. Izsák, F. Neese and D. Maganas, Accurate Band Gap Predictions of Semiconductors in the Framework of the Similarity Transformed Equation of Motion Coupled Cluster Theory, *Inorg. Chem.*, 2019, **58**, 9303-9315.
26. M. Liao, Z. Mu, Q. Wang, X. Zhang, H. Dong, M. Wen and F. Wu, Understanding the cyan-emitting phosphor $RbNa(Li_3SiO_4)_2$: Eu^{2+} by providing Rb ion vacancies, *J. Alloys Compd.*, 2020, **837**.
27. M. Liao, Q. Wang, Q. Lin, M. Xiong, X. Zhang, H. Dong, Z. Lin, M. Wen, D. Zhu, Z. Mu and F. Wu, Na Replaces Rb towards High-Performance Narrow-Band Green Phosphors for Backlight Display Applications, *Adv. Opt. Mater.*, 2021, **9**.
28. R. Shafei, D. Maganas, P. J. Strobel, P. J. Schmidt, W. Schnick and F. Neese, Electronic and Optical Properties of Eu^{2+}-Activated Narrow-Band Phosphors for Phosphor-Converted Light-Emitting Diode Applications: Insights from a Theoretical Spectroscopy Perspective, *J. Am. Chem. Soc.*, 2022, **144**, 8038-8053.
29. F. Neese, Prediction of molecular properties and molecular spectroscopy with density functional theory: From fundamental theory to exchange-coupling, *Coord. Chem. Rev.*, 2009, **253**, 526-563.
30. M. Atanasov, D. Ganyushin, D. A. Pantazis, K. Sivalingam and F. Neese, Detailed Ab Initio First-Principles Study of the Magnetic Anisotropy in a Family of Trigonal Pyramidal Iron(II) Pyrrolide Complexes, *Inorg. Chem.*, 2011, **50**, 7460-7477.
31. J. L. Jung, M. Atanasov and F. Neese, Ab Initio Ligand-Field Theory Analysis and Covalency Trends in Actinide and Lanthanide Free Ions and Octahedral Complexes, *Inorg. Chem.*, 2017, **56**, 8802-8816.
32. L. Lang, M. Atanasov and F. Neese, Improvement of Ab Initio Ligand Field Theory by Means of Multistate Perturbation Theory, *J. Phys. Chem. A*, 2020, **124**, 1025-1037.
33. S. K. Singh, J. Eng, M. Atanasov and F. Neese, Covalency and chemical bonding in transition metal complexes: An ab initio based ligand field perspective, *Coord. Chem. Rev.*, 2017, **344**, 2-25.

34. D. Yepes, F. Neese, B. List and G. Bistoni, Unveiling the Delicate Balance of Steric and Dispersion Interactions in Organocatalysis Using High-Level Computational Methods, *Journal of the American Chemical Society*, 2020, **142**, 3613-3625.
35. A. Meijerink and G. Blasse, Luminescence properties of Eu2+-activated alkaline earth haloborates, *J. Lumin.*, 1989, **43**, 283-289.
36. P. Dorenbos, Anomalous luminescence of Eu^{2+} and Yb^{2+} in inorganic compounds, *J. Phys.: Condens. Matter*, 2003, **15**, 2645-2665.